The chromatin remodeller CHD4 regulates transcription factor binding to both prevent activation of silent enhancers and maintain active regulatory elements

Andria Koulle[1,2,3], Oluwaseun Ogundele[1,2], Devina Shah[1,2,4], India-May Baker[1], Maya Lopez[1], Nicola Reynolds[1,5], Ramy Ragheb[1,5], Ernest Laue[1,2] and Brian Hendrich[1,2,5]

1. Cambridge Stem Cell Institute, Jeffrey Cheah Biomedical Centre, University of Cambridge, Cambridge CB2 0AW, UK
2. Department of Biochemistry, University of Cambridge, Cambridge CB2 1GA, UK

3. Current Address: Department of Life Sciences, Imperial College London, London, SW7 2AZ, UK
4. Current Address: University of Copenhagen, Novo Nordisk Foundation Center for Protein Research, Blegdamsvej 3B, 2200 Copenhagen, Denmark
5. Current Address: Living Systems Institute, University of Exeter, Exeter EX4 4QD, UK

All correspondence to Brian Hendrich: B.D.Hendrich@exeter.ac.uk

Abstract

Chromatin organisation and transcriptional regulation are tightly coordinated processes that are essential for maintaining cellular identity and function. ATP-dependent chromatin remodelling proteins play critical roles in control of genome structure and in regulating transcription across eukaryotes. Their essential nature, however, has made it difficult to define exactly how these functions are mediated. The chromatin remodeller CHD4 has been shown to be capable of sliding nucleosomes in vitro, and to regulate chromatin accessibility and gene expression in vivo. Using an inducible depletion system, here we identify a second mechanism of action for CHD4 in actively restricting the residence time of transcription factors on chromatin. Together these activities result in distinct, context-dependent outcomes: at highly accessible regulatory elements, CHD4 limits transcription factor binding to maintain regulatory function, while at low-accessibility euchromatic regions, it prevents transcription factor engagement and sustains chromatin compaction, thereby silencing cryptic enhancers. Collectively, these mechanisms enable CHD4 to reduce transcriptional noise while preserving the responsiveness of active regulatory networks.

Introduction

Cell state transitions are driven by the activity of transcription factors. Many transcription factors bind to specific DNA motifs within chromatin, but the frequency of these motifs within mammalian genomes far outnumbers sites at which protein binding is detectable. The ability of a transcription factor to recognise its cognate motif is influenced by how the DNA encoding that motif is packaged in chromatin. Accessible sites, i.e. those associated with a low density of intact nucleosomes, are more likely to be identified and bound by transcription factors than are inaccessible sites, i.e. those associated with higher nucleosome density. Controlling chromatin accessibility is therefore crucial for controlling transcription factor binding to cognate sites in regulatory regions. Transcription factor binding patterns will then determine which gene regulatory regions are used to drive gene expression and thereby define cell identity.

Vertebrate cells contain multiple proteins capable of using energy derived from ATP hydrolysis to remodel nucleosomes. These chromatin remodellers share a conserved sucrose non-fermentable 2 (SNF2) helicase-like ATPase domain but otherwise have various additional functional domains which impact how they organise chromatin, transcription and DNA repair (Hota and Bruneau, 2016; Narlikar et al., 2013). Chromatin remodellers play important roles

in mammalian development, and heterozygous mutations in the genes encoding them underlie a variety of developmental disorders in humans (Gourisankar et al., 2024; Hota and Bruneau, 2016; Pierson et al., 2019). Similarly, somatic mutations in chromatin remodeller subunit genes are increasingly being implicated in cancer initiation and/or progression (Lai and Wade, 2011; Martincorena et al., 2017; Wilson and Roberts, 2011).

CHD4 is an abundant ATP-dependent chromatin remodelling protein which plays important roles in chromatin organisation and cell fate decisions in many different aspects of metazoan development. Depletion of CHD4 in mouse or Drosophila cells, or overexpression of a dominant negative form of the protein, leads to increased chromatin accessibility at regulatory elements and DNase hypersensitive sites (Dieuleveult et al., 2016; Morris et al., 2014; Moshkin et al., 2012), indicating that it predominantly functions to compact chromatin. Its impact on gene expression is less clear-cut, however. One study found that while CHD4 acted to repress genes with bivalent promoters, its activity at active promoters (marked with H3K4Me3) mainly facilitated transcription in mouse embryonic stem cells (Dieuleveult et al., 2016). Another study found CHD4 controlled the probability of gene expression, rather than levels, during the first cell fate transition in mammalian embryogenesis (O'Shaughnessy-Kirwan et al., 2015). Several studies in somatic lineages have shown that CHD4 prevents lineage inappropriate gene expression during cell fate decisions in both mice and Drosophila (Arends et al., 2019; Aughey et al., 2023; Gómez-del Arco et al., 2016; Sreenivasan et al., 2021; Wilczewski et al., 2018; Yoshida et al., 2019). Exactly how CHD4 has this varied impact on chromatin and transcription has not been defined.

CHD4 is the predominant chromatin remodelling subunit of the Nucleosome Remodelling and Deacetylation (NuRD) complex (Wade et al., 1998; Xue et al., 1998; Zhang et al., 1998) . NuRD is a highly abundant chromatin remodeller present at active enhancers and promoters in many cell types. Its activity is important not only to regulate transcription but also the movement of enhancers in 3D space (Basu et al., 2023) , and to maintain genome integrity (Polo et al., 2010; Smeenk et al., 2010) . NuRD has been shown to exert two functions in mammalian cells: one is to control the nucleosome density at active enhancers, thereby regulating transcription factor binding, enhancer activity and transcriptional output (Bornelöv et al., 2018; Pundhir et al., 2023), while the other is to prevent low-level, inappropriate transcription across the genome (Burgold et al., 2019; Montibus et al., 2023; Ragheb et al., 2020; Saotome et al., 2024).

66 Although mouse ES cells can survive with a complete loss of the histone deacetylase
67 subunit of NuRD (Burgold et al., 2019), loss of the chromatin remodelling component, CHD4,
68 leads to cell death (Stevens et al., 2017). While we have used genetics to create NuRD-low or
69 NuRD-null ES cells in the past to define NuRD function, in both cases, the remodelling
70 subcomplex (CHD4, GATAD2A/B, CDK2AP1) remained on chromatin and the extent to which it
71 could continue to remodel chromatin is not known (Bornelöv et al., 2018). As with any genetic
72 change, it is also very difficult to know to what extent constitutive loss of protein activity has
73 resulted in selection of cells using some compensatory mechanism to remain viable. CHD4 is
74 also known to function outside of the NuRD complex (O'Shaughnessy-Kirwan et al., 2015;
75 Ostapcuk et al., 2018; Williams et al., 2004) . Assessing the direct function of NuRD's
76 remodelling activity is therefore difficult as knockout of the remodeller results in a non-viable
77 cell, while knockdown or exogenous overexpression of a dominant negative version of the
78 remodeller (Bornelöv et al., 2018; Feng and Zhang, 2001) will likely produce a heterogeneous
79 mix of cells with varying levels of remodeller activity and displaying increasing degrees of cell
80 cycle arrest and apoptosis over time.
81 The CHD4/NuRD function described at enhancers has been defined both in genetic
82 mutants and over a time course of NuRD reintroduction to null cells (Bornelöv et al., 2018;
83 Reynolds et al., 2012) . In contrast, the noise reduction function has been described in
84 genetically NuRD-deficient or NuRD-null cells or after NuRD component knockdown (Burgold
85 et al., 2019; Montibus et al., 2023; Ragheb et al., 2020; Saotome et al., 2024) , meaning that
86 this could either be a primary function of NuRD or a downstream consequence and/or cell
87 adaptation of NuRD deletion/depletion. For these reasons we have employed a degron
88 system, which allows us to acutely deplete CHD4 protein in mouse ES cells and assess the
89 consequences to chromatin and gene expression within minutes to hours of protein
90 depletion, long before the cells begin to exhibit cell cycle defects.
91
92 **Results**
93 **CHD4 has an immediate and widespread impact on chromatin accessibility**
94 NuRD in mouse ES cells can exist in various forms and it can contain different paralogs of
95 key components such as MBD2 or MBD3, GATAD2A or GATAD2B, HDAC1 or HDAC2, and
96 MTA1, 2 and/or MTA3 (Reid et al., 2023). In embryonic stem cells NuRD has only one
97 chromatin remodelling subunit: CHD4. We therefore created ES cell lines in which the
98 endogenous *Chd4* alleles were homozygously tagged with a mini-Auxin inducible degron

99 (mAID) (Nishimura et al., 2009). CHD4-mAID was largely depleted from both the nucleoplasm
100 and chromatin within 60 minutes of Auxin addition (Fig. 1A). CHD4 depleted cells showed a
101 normal cell cycle profile until 24 hours of depletion, when they began to undergo cell cycle
102 arrest at the G1/S checkpoint (Fig. 1B). By 30 hours CHD4-depleted cells were undergoing
103 apoptosis, which increased through 48 hours. We therefore focused our analyses on the first
104 few hours after CHD4 depletion, well before cells started to undergo cell cycle arrest.
105 CHD4 depletion had an immediate and widespread impact on chromatin accessibility, as
106 measured by calibrated ATAC-seq. After 60 minutes of CHD4 depletion there were more than
107 thirteen thousand sites showing a significant change in accessibility, which increased to over
108 fifty thousand sites showing increased accessibility and eight thousand showing decreased
109 accessibility by 4 hours (Fig. 1C). These data are consistent with previous reports of overall
110 increased accessibility upon CHD4/dMi2 depletion by shRNA in mouse ES cells or Drosophila
111 S2 cells (Dieuleveult et al., 2016; Moshkin et al., 2012).
112 Differentially accessible regions increasing in accessibility upon CHD4 depletion exhibited
113 low accessibility and low overall enrichment for specific histone modifications associated
114 with active chromatin in undepleted cells (H3K27Ac, H3K4Me1, H3K4Me3 (to an even lesser
115 extent), but not H3K27Me3; Fig. 1D,E). As a class, these sites predominantly mapped to
116 inactive enhancers and repetitive elements (Fig. 1F). They had very low average enrichment
117 for CHD4 or MBD3 (Fig. 1G) and would likely not pass the threshold to be counted as “Peaks”
118 in many ChIP-seq or Cut&Run datasets. Low enrichment for active chromatin marks and
119 NuRD components as well as low but detectable accessibility indicates that these sites
120 predominantly represent silent and cryptic regulatory sequences. Upon CHD4 loss
121 accessibility at these sites increased two- to three-fold at 60 and 240 minutes of depletion
122 (Fig. 1D) indicating that the low level CHD4 enrichment at these sites is nevertheless
123 functionally relevant.
124 Sites showing decreased accessibility without CHD4 were highly accessible in undepleted
125 cells, enriched for marks of active chromatin such as H3K4Me1 and H3K27Ac, and to a lesser
126 extent H3K4Me3 (Fig. 1D,E), and often overlapped with known enhancers and promoters
127 (Fig.1F). These sites also showed high enrichment for CHD4 and MBD3 in the undepleted
128 state (Fig. 1G). Upon CHD4 depletion accessibility at these sites was reduced by less than
129 two-fold on average (Fig. 1D). We and others have previously shown that NuRD acts at active
130 enhancers (Basu et al., 2023; Bornelöv et al., 2018; Dieuleveult et al., 2016) and, consistent
131 with these findings, CHD4 depletion caused an average decrease in accessibility at active

enhancers (Fig. 1H). We therefore conclude that CHD4 activity maintains closed chromatin generally at inactive regulatory sequences but also contributes to the maintenance of highly accessible chromatin at active sites.

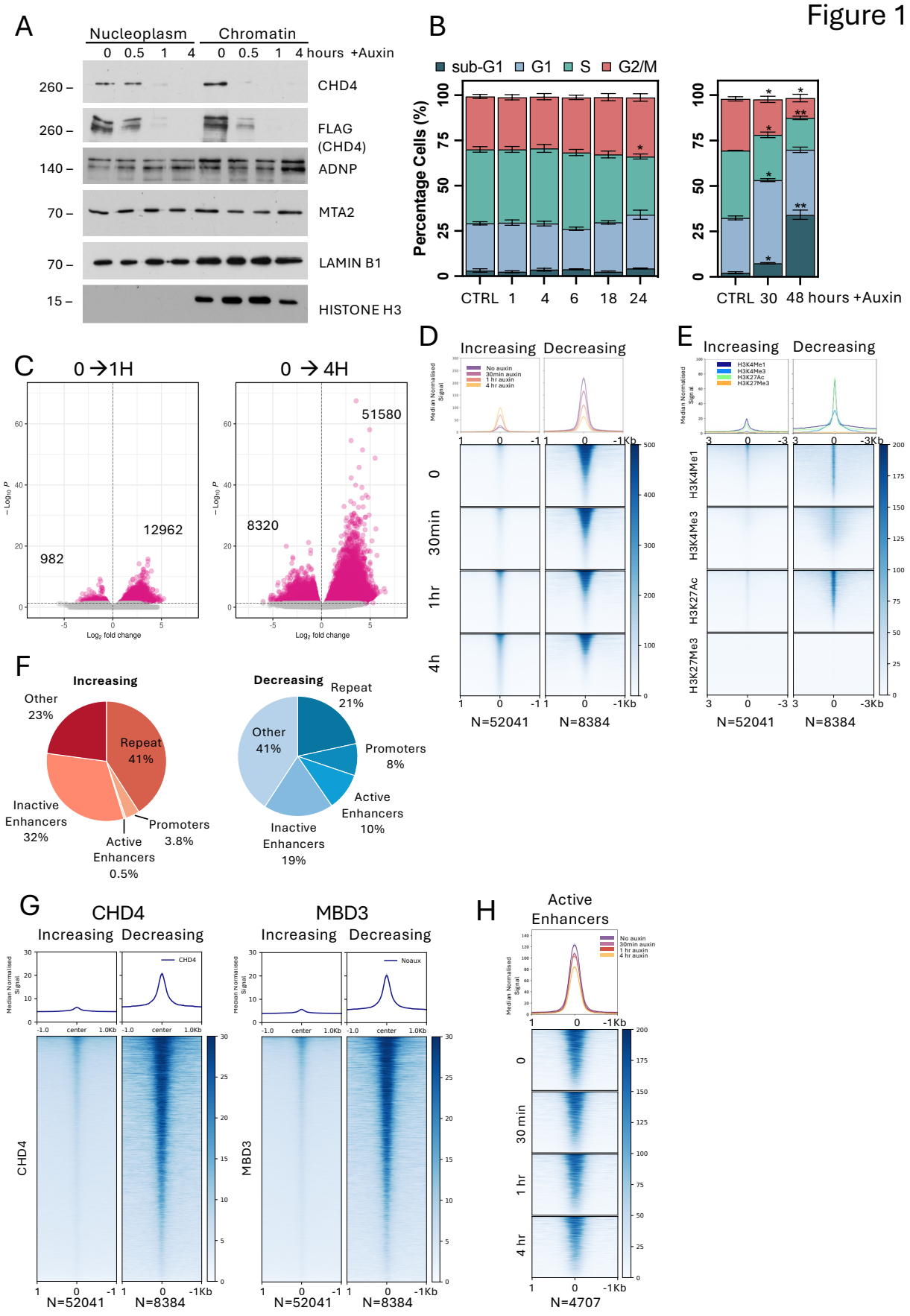

Figure 1. The impact of CHD4 depletion on chromatin accessibility. A. Western blots of nuclear soluble (Nucleoplasm) and chromatin fractions across CHD4 depletion probed with antibodies directed against indicated proteins. Times in hours of Auxin addition are indicated across the top. Lamin B1 and Histone H3 act as loading controls. **B**. Cell cycle analysis across CHD4 depletion time course. Hours post Auxin addition are indicated at the bottom, "CTRL" indicates DMSO control. Data represent an average of three replicates. Asterisks indicate significant differences from CTRL using a mixed-effects model with Dunnett's multiple comparisons correction. *$p < 0.05$; **$p < 0.01$. **C**. Volcano plots of differentially accessible ATAC-seq peaks between 0 and 1 hour of Auxin addition (left) or 0 and 4 hours of Auxin addition (right). Magenta spots indicate statistically significant differences (FDR > 0.05). Numbers of significant peaks decreased or increased are indicated on the plots. **D**. Heatmaps of ATAC-seq signal for all regions displaying increased accessibility (N=52041) or decreased accessibility (N=8384) at any time across the CHD4 depletion time course are displayed for each time point. **E**. Heatmaps of Cut&Run data for indicated histone modifications at sites increasing or decreasing in accessibility (as in panel **D**) (H3K27Ac and H3K4Me1 from this study; H3K27Me3 and H3K4Me3 taken from (Lando et al., 2024)) at indicated times after CHD4 depletion. **F**. Percentages of sites increasing in accessibility (top, blue) or decreasing in accessibility upon CHD4 depletion (bottom, red) which localise to indicated genomic features. Active enhancers are defined as having H3K4Me1 and K3K27Ac but not K3K4Me3, and inactive enhancers as having H3K4Me1 but not H3K4Me3 or H3K27Ac. **G**. Heatmaps of CHD4 and MBD3 Cut&Run data at upDARs and downDARs in 2iL conditions. **H**. Heatmaps of ATAC-seq signal at active enhancers (N=4707) across the CHD4 depletion time course.

CHD4 activity maintains expression of active genes while reducing transcriptional noise

Significant changes in gene expression were first detected in nascent and total mRNA 1-2 hours after CHD4 depletion (Fig. 2A,B). Loss of CHD4 resulted in an approximately 2:1 ratio of increased to decreased gene expression from 1 hour onwards (Fig. 2C), consistent with CHD4 activity able to both facilitate and limit transcription, with most genes changing by two-fold or less (Fig. 2D). GO terms associated with activated genes indicate various tissue-specific functions, consistent with the general noise reduction activity described for NuRD (Burgold et al., 2019; Montibus et al., 2023; Ragheb et al., 2020). Downregulated genes, in contrast, are associated with cellular maintenance and early development, consistent with these genes being normally highly expressed in ES cells (Fig. 2E).

To assess whether the observed changes in chromatin accessibility were linked to changes in gene expression, we plotted the distance between differentially accessible regions and the annotated TSS of genes found to be misexpressed up to 4 hours after CHD4 depletion. While most differentially accessible regions are located between 5 Kb and 100 Kb from the promoter of a differentially expressed gene, a notable number of sites losing accessibility are located within 1Kb of the TSS of misregulated genes (Fig. 3A). This indicates that CHD4 acts at highly active promoters to maintain both chromatin accessibility and transcriptional fidelity.

Sites increasing in accessibility upon CHD4 depletion tended to be located far from genes repressed by CHD4 (Fig. 3A). We therefore hypothesised that CHD4 depletion could activate silent or cryptic enhancers which could contribute to the increased transcriptional noise seen

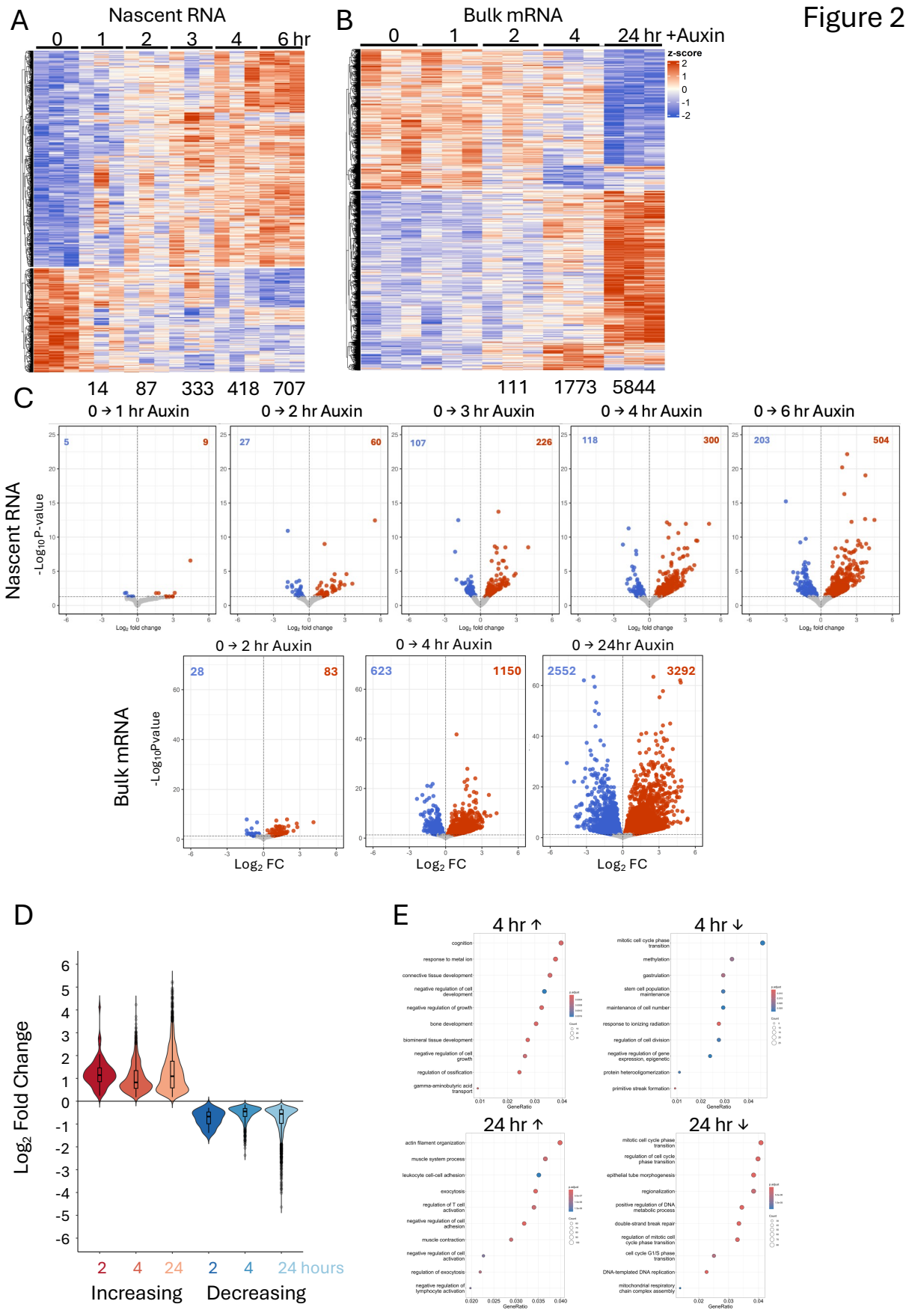

Figure 2. CHD4 acutely regulates gene expression. A and B. Heatmaps from nascent RNA-seq (A) or bulk RNA-seq (B) of genes showing significant (P_{adj} <0.05) changes in expression at any point during the CHD4 depletion time course. **C**. Volcano plots showing significant gene expression changes at indicated time points in nascent RNAseq (top) and bulk RNAseq (bottom). Genes increasing upon CHD4 depletion are shown in red, and those decreasing are shown in blue. The number of significantly misexpressed genes at each time point is indicated in the figure. **D**. Violin plots showing the average Log_2FoldChange of significant upregulated (red) and downregulated (blue) genes during the CHD4 depletion timecourse. **E**. Gene Ontology (GO) enrichment analysis of genes increased or decreased after four hours or 24 hours of CHD4 depletion. The top 10 biological processes are shown for each category, based on smallest adjusted p-value.

in NuRD mutant cells. Genes increasing in expression after four hours of CHD4 depletion were, on average, the nearest differentially expressed gene to twice as many sites increasing in accessibility than were genes decreasing in expression at the four hour time point (Fig. 3B). Though far from conclusive, this is consistent with the hypothesis that CHD4 prevents transcriptional noise by preventing activation of cryptic enhancers.

If loss of CHD4 resulted in activation of normally silent or cryptic enhancers, we would expect that they should show increases in enhancer-associated histone modifications and binding of transcription factors (TFs). As expected, Cut&Tag for H3K4Me1 and H3K27Ac showed increasing enrichment at upDARs 4 hours after CHD4 depletion, which did not increase further by 24 hours of depletion (Fig. 3C). Although these sites were largely unbound by NANOG or SOX2 in the presence of CHD4, within 1 hour of CHD4 depletion, upDARs became extensively bound by both transcription factors (Fig. 3D). Consistently, tens of thousands of new NANOG and SOX2 peaks were detected across the genome after CHD4 depletion (Fig. 3E). For example, the 25 kb region upstream of the *Eomes* gene contains multiple upDARs (Fig. 3F). Those labelled 1, 2 and 3 show very little, if any, accessibility or TF binding, and very low H3K27 acetylation and H3K4 monomethylation in undepleted cells. All three of these show a gain in accessibility, TF binding and both histone modifications upon CHD4 depletion. Those upDARs labelled 4 and 5 both show some accessibility, TF binding and enrichment for active histone modifications in undepleted cells. Nevertheless, these sites also show an increase in all of these features upon CHD4 depletion. In contrast, the nearby *Eomes* promoter ("P") shows little or no change in accessibility, TF binding or enrichment for H3K27Ac or H3K4Me1 across the CHD4 depletion time course.

We conclude that low-level association of CHD4 and NuRD across euchromatin restricts chromatin accessibility, preventing transcription factors from binding to consensus sequence

motifs. Failure to maintain this level of chromatin inaccessibility results in activation of inactive and/or cryptic enhancers, which drive inappropriate gene expression genome wide.

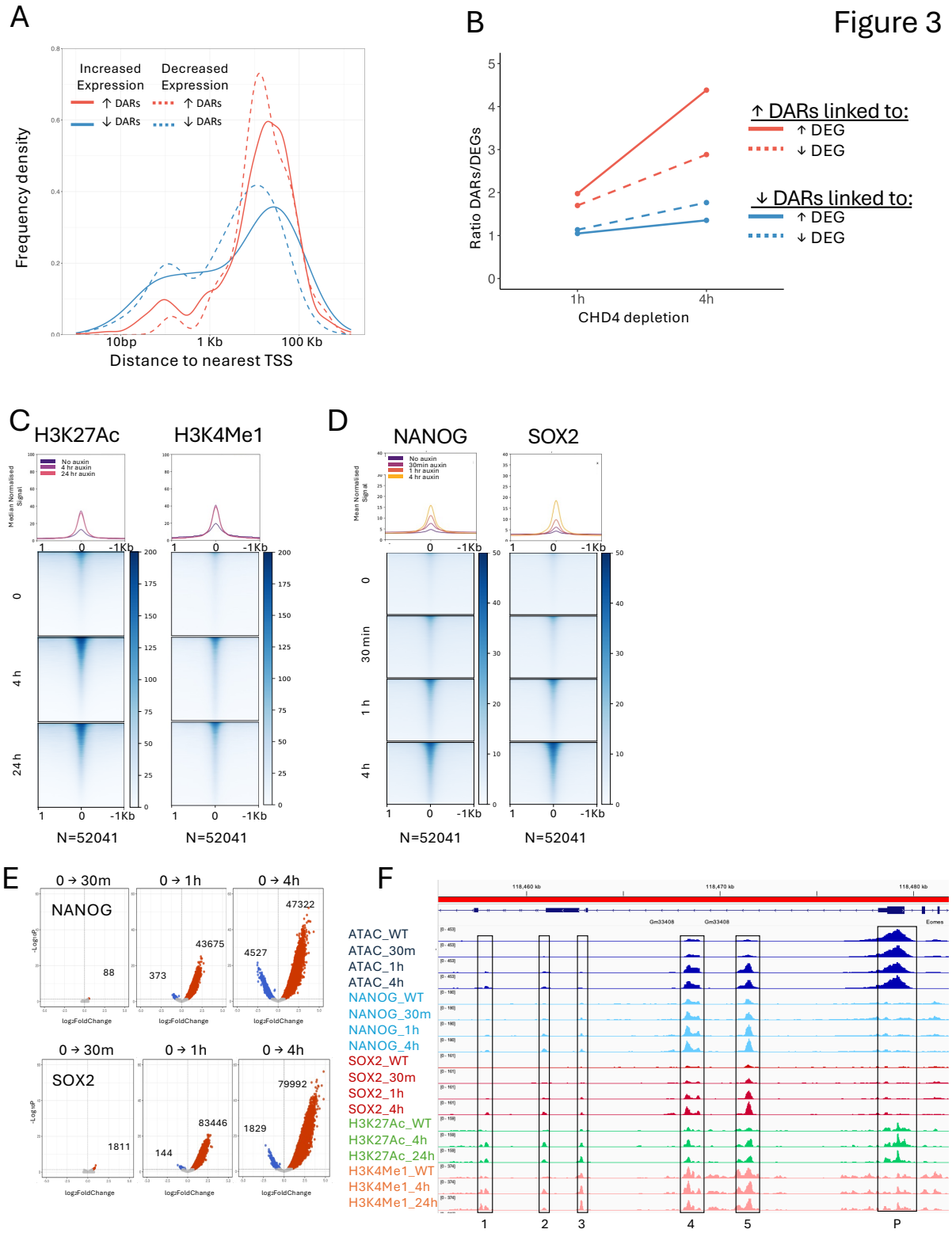

Figure 3. Chromatin opening upon CHD4 depletion. A. Frequency density distribution of the distance of increasing Differentially Accessible Regions ("upDARs;" red lines) and decreasing regions ("downDARs;" blue lines) to the TSS of genes showing increased (solid lines) or decreased (dotted lines) expression within four hours of CHD4 depletion. **B**. For genes either increasing or decreasing at each time point, we have plotted the average number of DARs for

which genes of that category were found to be the closest gene. **C**. Heatmaps of Cut&Tag signal for H3K27Ac, and H3K4Me1 at sites increasing in accessibility at indicated times of CHD4 depletion. **D**. Heatmaps of NANOG and SOX2 Cut&Run signal at increasing accessibility sites at indicated times of CHD4 depletion. **E**. Pairwise comparisons of called peaks of binding for NANOG (top) and SOX2 (bottom) between undepleted cells (0h) and 30 minutes, 1 hour or 4 hours of CHD4 depletion. Significantly changed (FDR>0.05) binding sites are shown in blue when $log_2FC>0$ and red when $log_2FC<0$. **F**. IGV screenshot of the upstream region of the mouse *Eomes* locus displaying ATAC-seq, Cut&Run and Cut&Tag data as indicated at left. Boxed regions labelled 1-5 are upDARs, while the box labelled P corresponds to the *Eomes* promoter.

CHD4 and SALL4 maintain chromatin inaccessibility largely independently

The SALL4 protein is a very abundant transcription factor in mouse ES cells, which has long been known to interact with the NuRD complex (Kloet et al., 2015; Lauberth and Rauchman, 2006; Lu et al., 2009; Miller et al., 2016). SALL4 preferentially binds to A/T-rich DNA genome-wide, where it is proposed to exert a general repression function through NuRD recruitment (Kong et al., 2021; Pantier et al., 2021; Ru et al., 2022; Watson et al., 2023). If this model is correct, we would expect some proportion of the CHD4 upDARs to be dependent upon both CHD4 and SALL4 to remain inaccessible. To test this model, we assessed chromatin accessibility after dTAG-mediated SALL4 depletion. SALL4 is partially redundant with SALL1 in ES cells, but only SALL4 is required for early mammalian development (Miller et al., 2016; Nishinakamura et al., 2001). We therefore created *Sall1*$^{-/-}$*Sall4*$^{FKBP/-}$ ES cells in which one endogenous *Sall4* allele was mutated and the remaining allele was targeted to express a SALL4-FKBP fusion protein.

Acute depletion of SALL4-FKBP resulted in rapid and extensive changes in chromatin accessibility as measured using ATAC-seq. Over 18,000 sites showed increased accessibility within 1 hour of SALL4 depletion in *Sall1*$^{(-/-)}$ ES cells (Fig. 4A,B). These sites showed moderate enrichment for SALL4 in undepleted cells, though less than that seen at active enhancers (Fig. 4C). When we compared these sites to those gaining in accessibility upon CHD4 depletion (upDARs), we find that only 4559 sites of the more than 52,000 CHD4 -dependent sites also show dependency upon SALL4 to maintain chromatin inaccessibility (Fig. 4D-F). This means that only 17.2% of SALL4-dependent sites also rely on CHD4 to prevent chromatin opening. Moreover, over 47,000 CHD4-dependent sites show neither SALL4 binding nor SALL4 dependence to remain inaccessible (Fig4. D-G). Similarly, over 20,000 SALL4-dependent sites show no change in accessibility upon CHD4 depletion, despite showing similar levels of enrichment for NuRD components as those dependent upon both SALL4 and CHD4 (Fig.

261 4E,H). Consistent with the proposed preference of SALL4 for binding to A/T-rich DNA, SALL4-
262 unique regions showed enrichment for SALL4 binding and a high A/T-content (53.9%) (Fig.
263 4D). CHD4-unique regions showed little if any SALL4 enrichment and a much lower A/T
264 content (44.2%), while those sites requiring both SALL4 and CHD4 to remain inaccessible
265 showed enrichment for NuRD components as well as SALL4 and displayed intermediate A/T
266 content (48.2%). Together, these data show that both CHD4 and SALL4 broadly restrict
267 chromatin accessibility across the genome, but that their activities overlap at only a relatively
268 small proportion of sites.

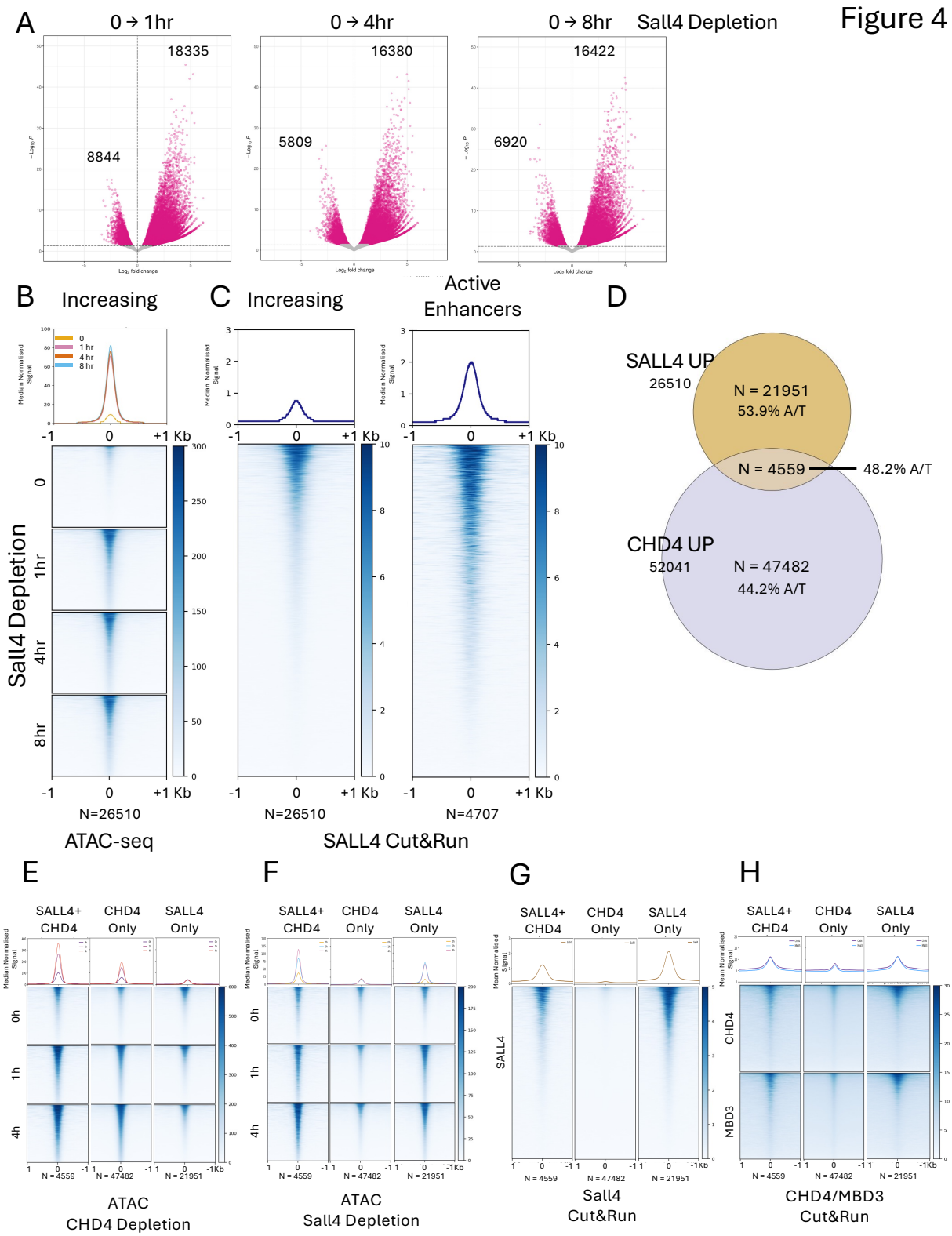

Figure4. CHD4 and SALL4 both restrict chromatin accessibility. A. Volcano plots of differentially accessible ATAC-seq peaks when comparing 1 hour, 4 hours or 24 hours of SALL4 depletion with those seen in undepleted cells (0). Magenta spots indicate statistically significant differences (FDR > 0.05). Numbers of significant peaks decreased or increased are indicated on the plots. **B**. Heatmaps of ATAC-seq signal for all regions displaying increased accessibility (N=26510) across the SALL4 depletion time course are displayed for each time point. C. Heatmap of SALL4 Cut&Run signal in undepleted ES cells (taken from (Ru et al., 2022)) at all regions displaying increased accessibility across the SALL4 depletion time

course (left, N=26510) or at active enhancers (right, N=4339). D. Overlap of sites showing increased accessibility upon SALL4 depletion with those increasing upon CHD4 depletion (upDARs). The % A/T base composition of the different categories of sites is indicated. **E, F**. Heatmaps of ATAC-seq signal at sites increasing upon either SALL4 or CHD4 depletion (SALL4+CHD4), sites increasing upon CHD4 depletion but not upon SALL4 depletion (CHD4 Only), or sites increasing upon SALL4 depletion but not upon CHD4 depletion (SALL4 Only) plotted at indicated time points of CHD4 depletion (**E**) and SALL4 depletion (**F**). **G, H**. Cut&Run signal for SALL4 (**G**) or for CHD4 and MBD3 (**H**) in undepleted ES cells at the three different classes of sites.

NuRD limits transcription factor binding to chromatin

Sites decreasing in accessibility upon CHD4 depletion showed an increase in enrichment for both NANOG and SOX2 after 30 minutes, even though these sites were, on average, losing accessibility and losing enrichment for the active chromatin marks H3K4Me1 and H3K27Ac at that time (Fig. 5A,B). Active enhancers similarly showed an increase in NANOG and SOX2 enrichment from 30 minutes of CHD4 depletion (Fig. 5C). An example locus is shown in Figure 5D, where a cluster of enhancers located 50-70Kb downstream of the *Klf4* gene contains several high accessibility sites. Those located at 68, 57 and 55 Kb away downstream of *Klf4* (labelled 68, 57 and 55, respectively in Figure 5D) all show a loss of ATAC-seq signal but a gain in NANOG and SOX2 enrichment from 30 minutes of CHD4 depletion.

The simultaneous decrease in chromatin accessibility and increase in transcription factor enrichment upon acute CHD4 depletion could indicate that CHD4/NuRD plays a direct role in controlling transcription factor binding to chromatin. To independently assess the impact CHD4 has on transcription factor binding, we used single molecule imaging in live ES cells to directly measure transcription factor binding kinetics upon CHD4 depletion. A HALO-Tag cassette was knocked-in to the endogenous *Nanog*, *Klf4* or *Sox2* loci in the CHD4-mAID ES cell line to create strains expressing the different C-terminal protein fusions. Single HALO-tagged protein molecules were then labelled with a photoactivatable dye (PA-JF646, (Grimm et al., 2016) and tracked at two distinct temporal regimes (where we collected images either every 20 ms or 500 ms), using double-helix point spread function (DH PSF) microscopy as they moved within a 4-μm slice of the nucleus. Recording at a 20 ms time resolution allows

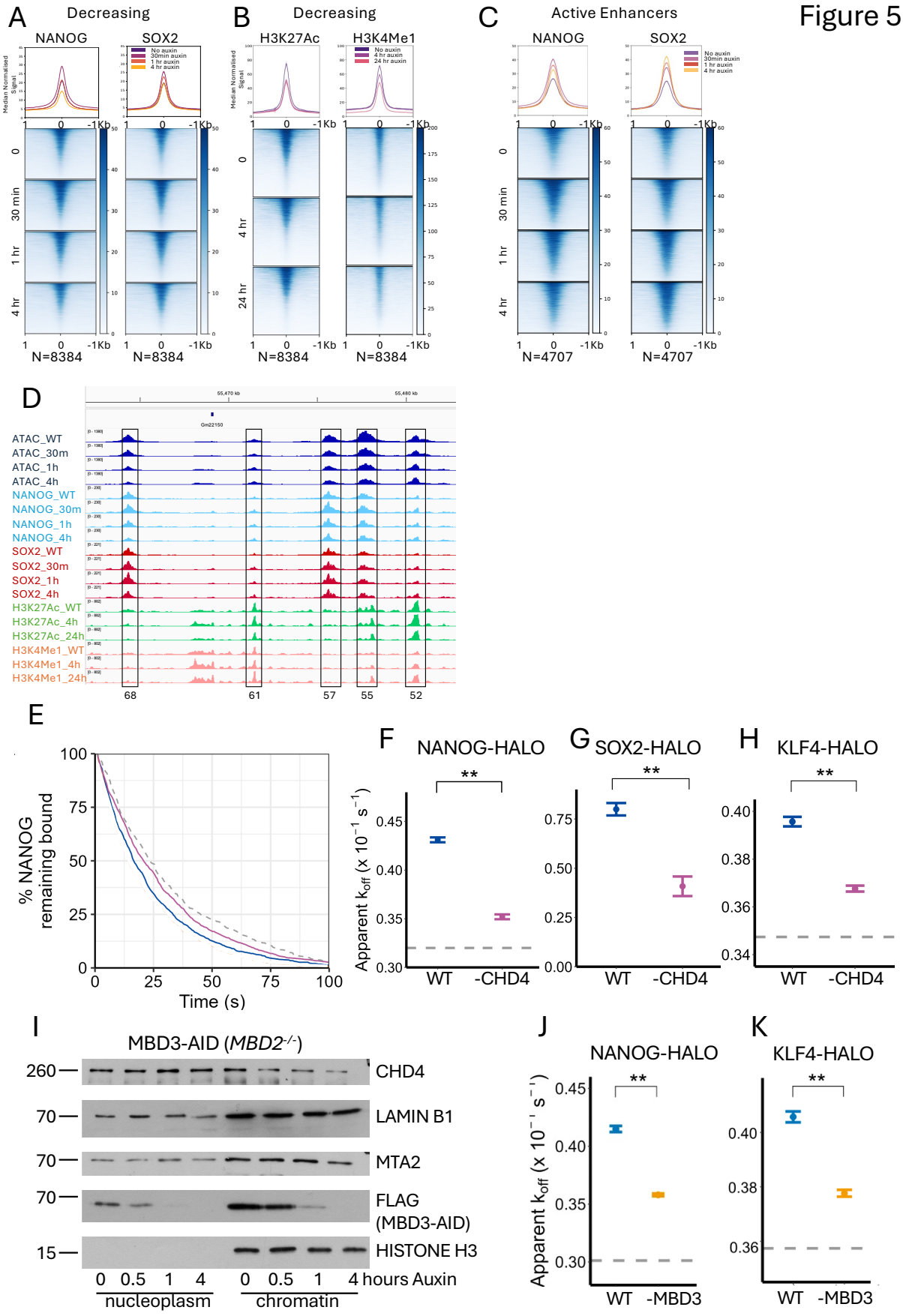

Figure 5. NuRD regulates NANOG and SOX2 binding to active sites. A. Heatmaps of NANOG and SOX2 Cut&Run signal at indicated times of CHD4 depletion across sites decreasing in accessibility. **B**. Heatmaps of H3K27Ac and K3H4Me1 Cut&Tag signal at indicated times of CHD4 depletion across decreasing accessibility sites. **C**. Heatmaps of

Cut&Run signal for NANOG and SOX2 across active enhancers at indicated times of CHD4 depletion. **D.** IGV screenshot of the enhancer cluster downstream of the *Klf4* gene displaying ATAC-seq, Cut&Run and Cut&Tag data as indicated at the left. Boxed regions are labelled with the distance in Kb from the annotated *Klf4* transcription start site. **E**. Fluorescence survival curves of chromatin-bound NANOG-HALO molecules in 2iL (blue line) or after 1 hour of CHD4 depletion (purple line). The grey dotted line represents the fluorescence survival curve for molecules in a fixed-cell control imaged under identical conditions. **F**. Apparent dissociation rates (k_{off}) of chromatin-bound NANOG molecules calculated through fitting a single exponential decay model to the survival curves in **panel E**. Error bars represent 95% confidence intervals for each fit applied to data taken from three independent experiments. The horizontal dashed line represents the upper 95% confidence limit for a fixed-cell control. ** indicates that 99% confidence intervals do not overlap, i.e. $p < 0.01$. **G.H**. As in **F** but for SOX2 (**G**) and KLF4 (**H**). The fixed cell control was not imaged in the SOX2 experiments in panel **F**. **I**. Western blots of nuclear soluble (Nucleoplasm) and chromatin fractions across MBD3 depletion probed with antibodies directed against the indicated proteins. Times in hours of Auxin addition are indicated across the top. Lamin B1 and Histone H3 act as loading controls. **J, K.** Apparent dissociation rates (K_{off}) for NANOG-HALO (**I**) and KLF4-HALO (**J**) before and after 60 minutes of MBD3 depletion. For calculation of K_{off} the trajectories were pooled from 4 replicates of each time point obtained over 2 days.

the segmentation of trajectories into freely diffusing and chromatin-bound states, and this data can be used to extract the chromatin binding kinetics of proteins and complexes (Basu et al., 2023) . Here, we used this data to determine residence times – how long the molecules remain bound to chromatin. The proportion of molecules that remain bound to chromatin after increasing lengths of time was then plotted before and after CHD4 depletion (for 1 hour) and the results were fitted with a single exponential decay to determine the apparent dissociation rate, k_{off} (Fig. 5E). NANOG-HALO, SOX2-HALO and KLF4-HALO all showed a pronounced decrease in apparent K_{off} after CHD4 depletion (Fig. 5F-H), consistent with CHD4 actively limiting transcription factor residence times on chromatin.

To determine whether it is CHD4 by itself or the intact NuRD complex that can remodel transcription factor binding, we similarly imaged NANOG-HALO and KLF4-HALO in MBD3-depletable ES cells after disruption of the NuRD complex (Fig. 5I). These cells were also null for *Mbd2*, which encodes a protein displaying partial functional redundancy with MBD3 but is dispensable in ES cells (Hendrich et al., 2001). As CHD4 is largely responsible for the binding of NuRD to its target enhancers, removal of MBD3 enables disassembly of NuRD, but does not prevent CHD4 binding to chromatin (Basu et al., 2023; Bornelöv et al., 2018; Zhang et al., 2016). The nucleosome remodelling activity of CHD4 is, however, greatly reduced outside of NuRD (Bornelöv et al., 2018). We therefore reasoned that if it is intact NuRD that is required (as opposed to just CHD4), depletion of MBD3 should also limit TF residence times. Indeed,

353 we detected a significant decrease in the apparent k_{off} of stably bound NANOG and KLF4 after
354 1 hour of MBD3 depletion (Fig. 5J,K). We therefore conclude that it is intact NuRD (and not
355 CHD4 by itself) that actively limits transcription factor residence times on chromatin, while at
356 the same time contributing to the maintenance of chromatin accessibility at active regulatory
357 regions.
358
359 **NuRD activity influences active and inactive regulatory elements differently**
360 We next asked how CHD4 activity could have different impacts on accessibility at different
361 kinds of sequences. Information about the structure of accessible regions can be obtained
362 from ATAC-seq data by quantitating recovered fragments of all sizes and determining the
363 frequency and location of recovered Tn5 integration sites using VPlots, (Henikoff et al., 2011;
364 Schep et al., 2015; Serizay and Ahringer, 2021)(Supplementary Figure 2). Applying this
365 analysis at sites increasing in accessibility upon CHD4 depletion shows an increase in both
366 Tn5 integrations and in reads corresponding to the nucleosome-free region (NFR) at the 30-
367 minute time point (Fig .6A,B). After 60 minutes, when CHD4 is almost completely depleted,
368 there is an increase in accessibility generally across the entire site, both of short reads within
369 the NFR but also longer reads (200-300bp) extending from the NFR outwards (Fig. 6B). We
370 conclude that NuRD is acting to restrict accessibility of both the NFR and of the flanking
371 nucleosomal DNA (see Supplementary Figure 2) at these sites, consistent with the
372 demonstrated role of CHD4/NuRD in maintaining the density of intact nucleosomes (Bornelöv
373 et al., 2018; Dieuleveult et al., 2016; Moshkin et al., 2012).
374 The example of the *Eomes* locus (Fig. 3F) illustrates that some CHD4-condensed sites
375 show a degree of accessibility in the presence of CHD4, while others show little if any
376 accessibility. To better understand how CHD4 prevents chromatin opening at these two
377 different kinds of sites, we constructed Tn5 integration plots and Vplots from the 1000
378 increasing sites showing the least accessibility in undepleted conditions and from the 1000
379 showing the most accessibility (Fig. 6C-F). Sites showing little or no accessibility in
380 undepleted cells initially show very few reads less than 100bp. The V-plots also show reads of
381 200-300 bp distributed across the regions, again indicative of generally inaccessible
382 chromatin. Loss of CHD4 results in the formation and progressive expansion of an NFR, as
383 well as an increase in longer reads with one end located within the NFR (Fig. 6C,D). The Tn5
384 integration plot does not show a general widening of the NFR over time, indicating that CHD4
385 function is largely focussed on maintaining nucleosome density within a 100-200bp region

386 (Fig. 6C). Sites at which CHD4 activity restricts accessibility at already accessible sites
387 showed a general increase in both small and longer reads as CHD4 was depleted, and a
388 broadening of the existing NFR (Fig. 6 E,F). Together these data are consistent with
389 CHD4/NuRD maintaining chromatin compaction at inactive or low activity enhancers by
390 maintaining nucleosome density. The sites at which CHD4 activity maintains accessibility
391 displayed a prominent NFR as well as high density of longer reads in undepleted cells (Fig.
392 6G,H). CHD4 depletion induced a general decrease in Tn5 integrations and VPlot signal
393 intensity across the site, consistent with CHD4 acting to generally maintain accessibility
394 across these sites.
395 We next asked why CHD4 promoted accessibility at highly accessible active sites (e.g. Fig6.
396 G,H) but reduced accessibility at slightly less accessible, inactive sites (e.g. Fig6 E,F). We took
397 advantage of ES cells in which a tamoxifen-inducible MBD3b is expressed in an otherwise
398 *Mbd3*-null ES cell line, allowing us to restore NuRD activity to cells upon tamoxifen addition
399 (Bornelöv et al., 2018; Reynolds et al., 2012). We had previously subjected these cells to
400 micrococcal nuclease (MNase) sequencing at different time points after MBD3 induction to
401 show that restoration of NuRD activity caused increased density of intact nucleosomes
402 across sites of active transcription (Bornelöv et al., 2018). Unlike ATAC-seq, sequencing of
403 MNase-treated DNA results in increased reads at sites protected from digestion by bound
404 proteins, i.e. less accessible regions, and a decrease in signal at locations where the DNA is
405 easily accessible and therefore digested by the MNase. In that study, we used an MNase
406 concentration at which DNA associated with intact nucleosomes is protected from MNase
407 digestion. Lower MNase concentrations, however, will recover DNA protected by other
408 chromatin proteins as well as by partial (fragile) nucleosomes (Kubik et al., 2015; Xi et al.,
409 2011).
410 We therefore subjected cells undergoing the time course of NuRD reformation to lower
411 MNase concentrations prior to sequencing. Traditional MNase sequencing shows that NuRD
412 increases the density of intact nucleosomes at both classes of accessible sites, as indicated
413 by an increase in signal from the red line (NuRD-deficient) to the black line (24h NuRD
414 restored) in the top panels of Figure 6I. This effect is more more pronounced at the most
415 accessible inactive sites ("UP Most Accessible", black line, Fig. 6I), occurring across a broader
416 area than at fully active sites ("All Decreasing", black line). The lower MNase concentration, by
417 contrast (Fig. 6I, lower panels) produces a peak of MNase resistance in the absence of NuRD
418 activity at both classes of sites (red lines), indicating an accumulation of structures which are

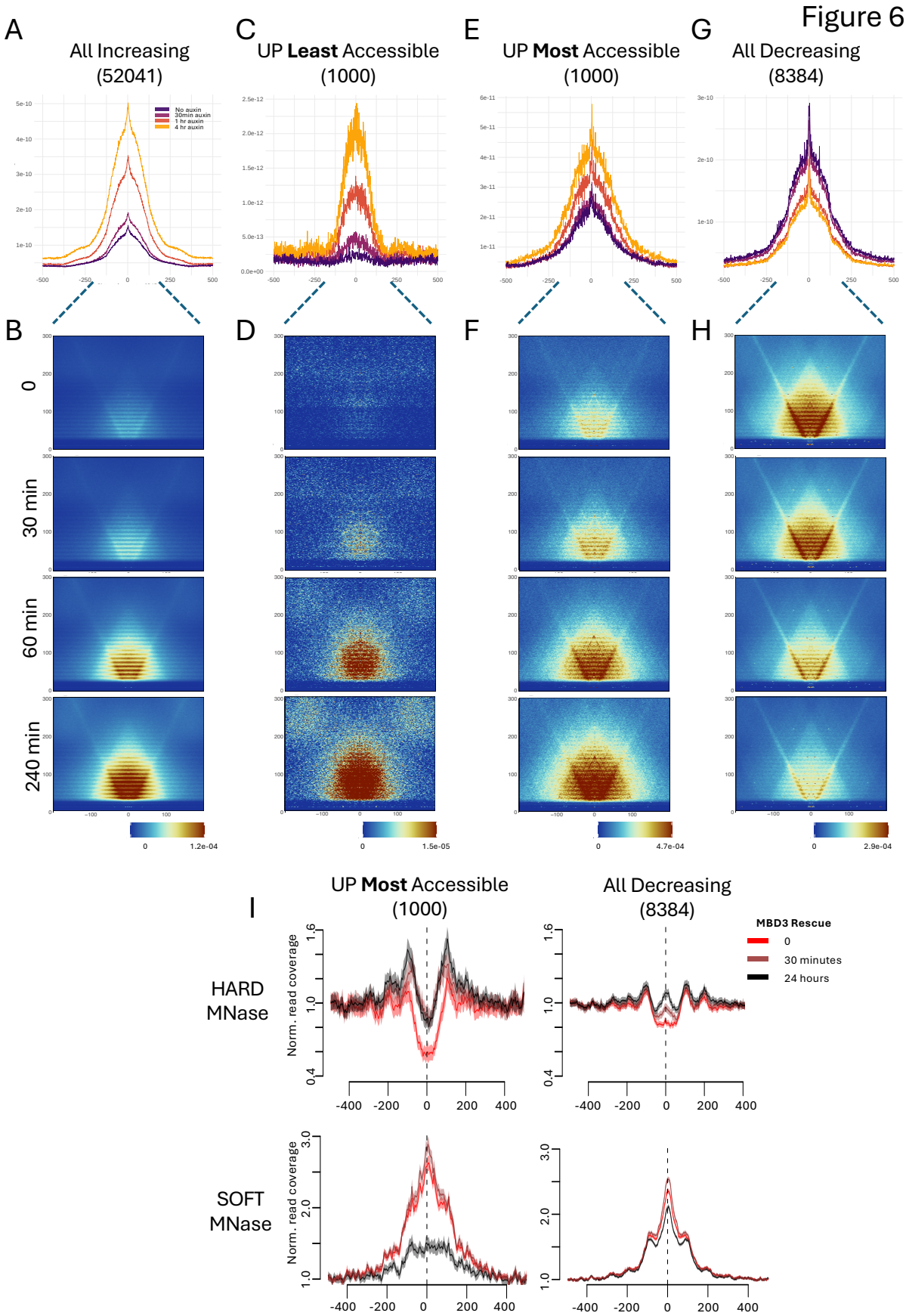

Figure 6. CHD4 controls accessibility differently at different classes of sites. A,C, E, G Tn5 integration frequency was determined from ATAC-seq data and plotted across indicated sites across the CHD4 depletion time course. The number of sites is shown in parentheses. **B, D, F, H** Vplots across sites indicated above (corresponding to the Tn5 integration plots) at indicated

times of CHD4 depletion. See **Supplementary Figure 2** for a Vplot schematic. **I.** MNase-seq data collected 0 (red), 30 minutes (dark red) or 24 hours (black) after of NuRD reformation in *Mbd3*$^{-/-}$ ES cells are plotted across indicated sites. Top graphs show results from "Hard" MNase treatment while bottom graphs show "Soft" MNase treatment (see text). The y-axis shows normalised read coverages, while the X-axis shows distance in base pairs from the centre of the feature. Curves show mean and standard error from 3 biological replicates.

digested by the higher MNase concentration, such as fragile nucleosomes. Restoration of NuRD activity clears the majority of this signal in at the most accessible inactive sites, but only moderately reduces their abundance at fully active sites (Fig. 6I, lower panels). These data indicate that at highly active regions, NuRD acts to limit the abundance of fragile nucleosomes and other proteins, while marginally increasing the density of intact nucleosomes, which has an overall result of maintaining these sites in a fully active state. It does not completely remove the fragile nucleosomes from these sites, which are presumably being created by the activity of other chromatin remodellers (Klein et al., 2023; Nocente et al., 2024). In contrast, at accessible but inactive sites it prevents the accumulation of fragile nucleosomes which would otherwise cause further opening and enable activation of inactive regulatory elements.

Together, these data show that CHD4 shows two modes of binding on chromatin: in addition to the high enrichment seen at active enhancers and promoters, it also shows low-level binding at silent and/or cryptic regulatory elements across euchromatin. At the former class of sites, it acts to limit the residence times of chromatin-associated proteins to maintain highly accessible chromatin. This maintenance activity of CHD4/NuRD is necessary for the full activity of these elements to direct appropriate transcription of target genes. At the latter class of sites it maintains chromatin in an inaccessible state, preventing accumulation of fragile nucleosomes and preventing transcription factors from recognising and stably binding their cognate motifs and thereby prevents spurious activation of these elements.

Discussion

Assessing CHD4 function by traditional knockout experiments is difficult as ES cells without CHD4 undergo cell cycle arrest and begin to apoptose after 24 hours (Fig. 1B). Even with siRNA or inducible deletion, cells in a population will lose CHD4 at different times and, in the case of siRNA, to different extents, making primary function difficult to ascertain. Genetic deletion in mouse ES cells has been used extensively to define protein function in cells and in intact mice. In such an experiment the genetic lesion will often be induced in a single cell, and

459 a clone of cells will be grown out from that single cell. While this is an extremely powerful
460 method for defining gene function, there is usually a very large number of cell divisions
461 occurring and considerable time passing between loss of the gene and assessment of
462 phenotype, making it of limited use when studying proteins required for the viability of ES
463 cells. Resulting phenotypes may be due directly to the absence of protein function but may
464 also reflect adaptations made by cells selected to proliferate in the absence of that protein.
465 The advent of inducible depletion methods (summarised in (Wit and Nora, 2023)) has meant
466 we can now infer protein function by assessing the immediate molecular consequences of
467 loss of a given protein activity in the very short term. Combined with genome-wide profiling,
468 this has allowed us to identify both a novel transcription factor remodelling activity for CHD4
469 and to define how this combines with the protein's nucleosome remodelling activity to exert
470 different functions at different classes of sites.

471 CHD4 is an abundant chromatin remodeller with a well-defined function in moving intact
472 nucleosomes. Here we show that CHD4 can also actively limit the residence times of
473 transcription factors on chromatin. The combination of these two activities has different
474 consequences at different kinds of sequences. At highly accessible, active sites (Fig. 7A)
475 CHD4 enrichment is high and it acts to limit the binding of transcription factors and fragile
476 nucleosomes to regulatory regions, allowing for full accessibility and functionality of these
477 regulatory elements. At inactive, less accessible euchromatic sites (Fig. 7B) CHD4 associates
478 more infrequently, but here it's TF removal activity, combined with maintenance of
479 nucleosome structure, is sufficient to keep accessibility low and to prevent transcription
480 factors from stably binding recognition motifs. This activity is sufficient to prevent the binding
481 of NANOG and SOX2, the latter being capable of binding nucleosomal templates (Dodonova
482 et al., 2020; Zhu et al., 2018). By combining these two activities, CHD4 functions to prevent
483 spurious activation of cryptic and/or silent regulatory regions, thereby reducing
484 transcriptional noise, but also acts to facilitate the activity of highly accessible regulatory
485 regions, allowing cells to accurately and rapidly respond to differentiation cues (Fig. 7).

486 Many transcription factors recognise and bind to specific sequence motifs in DNA. A
487 transcription factor recognising a 7 base pair sequence should, on average, have more than
488 150,000 different potential binding sites in a mammalian genome. Yet ChIP-seq and Cut&Run
489 studies have found most transcription factors associate with orders of magnitude fewer sites
490 in any one cell type (Lambert et al., 2018; Srivastava and Mahony, 2020). Most transcription
491 factors bind preferentially or exclusively in accessible chromatin, so it is believed that

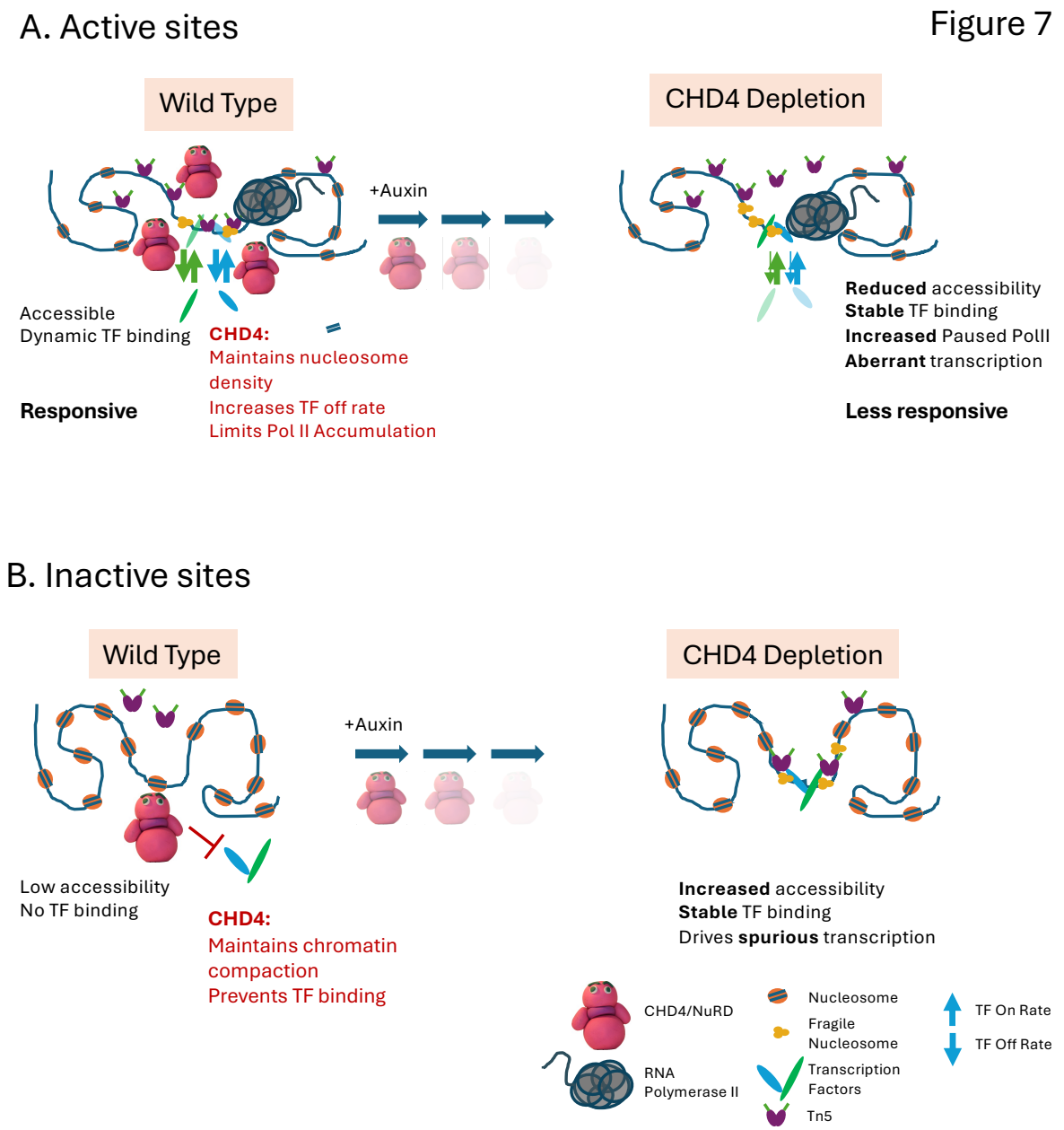

Figure 7. Model of CHD4 function. **A. Highly accessible sites.** In undepleted cells these sites are extensively bound by CHD4/NuRD, where it acts to promote the off rate of transcription factors to promote accessibility. Tn5 is able to access the central NFR but also can integrate into the flanking nucleosomal DNA. After CHD4 depletion, the on rate for TFs does not change, but the off rate is now much reduced, resulting in increased TF binding. The sites become less accessible to Tn5, such that although it can still access the hypersensitive site within the NFR, there are fewer integrations extending outwards. These regulatory regions cannot quickly respond to receipt of external signals. **B**. Model of CHD4 function at inaccessible, silent enhancers. In undepleted conditions, there is low CHD4 enrichment at these sites. Here, CHD4 acts to prevent binding of transcription factors and maintain low accessibility, such that Tn5 cannot frequently access the DNA. After CHD4 depletion, the locus becomes more accessible, and transcription factors can stably bind. This leads to spurious activation of distal promoters and an increase in transcriptional noise.

differences in chromatin accessibility, or nucleosome positioning across sites, determines which subset of the potential consensus DNA binding motifs are available for TF binding at

509 any given time or cell type (Workman and Buchman, 1993; Zhu et al., 2018). Here we identify
510 CHD4 as one factor which acts to prevent transcription factors, even so-called Pioneer
511 Factors, from binding thousands of sites in inaccessible chromatin. CHD4's chromatin
512 remodelling activity keeps the sites inaccessible, so TF binding is not favoured, and the ability
513 of CHD4 to remove TFs from chromatin means that even if they are capable of binding to a
514 nucleosomal substrate, CHD4 promotes their dissociation from chromatin so they are quickly
515 removed (Fig. 7B). At highly accessible chromatin, CHD4 is similarly limiting TF residence
516 times by increasing K_{off}, however, here accessibility is high so the K_{on} is also high. We propose
517 that here CHD4 activity facilitates the turnover of bound molecules (Fig. 7A). Without CHD4,
518 K_{off} decreases while K_{on} remains high, resulting in more stable binding of TFs to chromatin.
519 CHD4 and NuRD have been shown to be important for cells to properly respond to
520 differentiation cues in a wide variety of organisms and contexts (Ahringer, 2000; Bracken et
521 al., 2019; Lenz and Brehm, 2023; McDonel et al., 2009; Signolet and Hendrich, 2015) and we
522 propose that by facilitating TF turnover and accessibility at promoters and enhancers, CHD4
523 and NuRD facilitate the ability of regulatory elements to respond to differentiation cues (Fig.
524 7).
525 CHD4's activity to prevent spurious TF binding and chromatin opening occurs at many sites
526 where enrichment of CHD4 by ChIP or Cut&Run is low, but not absent. In contrast, at sites
527 showing high levels of CHD4 enrichment, the consequences of its activity to facilitate active
528 transcription. SALL4 presents another example of a protein exerting function away from its
529 predominant sites of chromatin enrichment: initial ChIP-seq results indicated that SALL4 was
530 predominantly located at enhancers, whereas more recent Cut&Run data indicates a wider
531 spectrum of sites bound by SALL4 (Kong et al., 2021; Miller et al., 2016; Pantier et al., 2021; Ru
532 et al., 2022). We find that SALL4 shows lower enrichment at A/T-rich genomic sites than it
533 does at enhancers, but that it nevertheless has a major impact on chromatin compaction at
534 these genomic A/T-rich sites (Fig. 4). While many groups, including ours, have generally
535 assumed protein function would be focussed at ChIP-seq "peaks," the current work
536 demonstrates that focusing on protein enrichment levels on chromatin is not necessarily the
537 best way to identify important sites of protein activity.
538 Together, our data show that CHD4 exerts functions on chromatin beyond its well-
539 described ability to slide intact nucleosomes along the DNA (Zhang et al., 2016; Zhong et al.,
540 2020) . Consistent with this conclusion, a recent paper found that acute depletion of CHD4
541 resulted in an increase in fragile nucleosomes at enhancers (Nocente et al., 2024), while we

542 and others have found that NuRD acts to limit the amount of paused RNA Polymerase II found
543 at active promoters (Bornelöv et al., 2018; Pundhir et al., 2023). It is possible that CHD4
544 translocates along the DNA within accessible sequences and physically displaces any
545 unstably bound proteins, such as transcription factors or fragile nucleosomes, that might be
546 in its way. Such activity might not be necessary at completely closed sites, but at inactive
547 enhancers showing a small amount of accessibility, infrequent binding and translocation of
548 NuRD across the accessible region could remove any proteins which have managed to bind.
549 The residence times of transcription factors vary but are generally on the order of a few
550 seconds (Lu and Lionnet, 2021). Why might it be important to limit the residence times of
551 transcription factors? We propose that this could fix an enhancer into a specific state, when
552 one important job of enhancers is to be responsive to changes in stimuli. If no change in
553 status quo is required, then after CHD4 promotes eviction of a particular transcription factor
554 from the enhancer it can continually re-bind and exert its influence over that enhancer.
555 Should signals change, the enhancer needs to be able to remove TFs corresponding to the old
556 signal to make space for determinants of the new signal. In this model, CHD4/NuRD
557 maintains this fluidity of transcription factor interactions, ensuring enhancers are rapidly able
558 to respond immediately upon receipt of differentiation cues.
559

560 **Methods**

561 **Mouse embryonic stem (ES) cells**

562 Mouse ES cells were cultured in 2i+LIF media on gelatin-coated plates (Montibus et al.,
563 2023; Mulas et al., 2019). All cell lines were genotyped and tested for mycoplasma regularly.
564 The CHD4-mAID ES cell line was made in BC8, an F1 hybrid from a C57Black/6 and Mus
565 castaneus cross (40, XY), obtained from Anne Ferguson-Smith (Cambridge). MBD3-AID ES
566 cells were created in 23AF, a primary ES cell line derived from *Mbd2*$^{-/-}$, *Mbd3*$^{Flox/Flox}$ mice (40,
567 XX) in a mixed C57Black/6 and 129/Ola background. Sall4-FKBP cells were created in *Sall1*$^{-/-}$
568 *Sall4*$^{+/-}$ ES cells (Miller et al., 2016).

569 Targeting constructs were made using the AID sequence (Nishimura et al., 2009) or mini-
570 AID (Kubota et al., 2013) amplified from an Oct4-AID plasmid; a gift from José Silva (Bates et
571 al., 2021) . Targeting plasmids using the FKBP protein (Nabet et al., 2018) were made by
572 amplifying FKBP from pLEX_305-C-dTAG; a gift from James Bradner & Behnam Nabet
573 (Addgene plasmid # 91798). Plasmids created as part of this study are available from
574 Addgene.

575 To create Auxin-depletable cell lines, parent lines were first transfected with a PiggyBac
576 construct to constitutively express OsTir1 (created using pMGS56 (GFP-ARF16-PB1-P2A-
577 OsTIR1); a gift from Michael Guertin (Addgene plasmid # 129668)) linked to either G418 or
578 Hygromycin resistance, and cells were cultured under selection to maintain OsTir1
579 expression. To create degron knock-ins, cells were lipofected with a targeting vector and
580 appropriate gRNA (Table 1) in a Cas9-expression vector (pSpCas9(BB)-2A-GFP (PX458); a gift
581 from Feng Zhang; Addgene plasmid # 48138). Drug resistant colonies were genotyped and
582 correctly targeted clones were subsequently transiently transfected with an expression
583 plasmid for Dre recombinase to remove ROXed drug selection cassettes. *Chd4* targeting
584 required two rounds of transfection, selection, and drug removal, while *Mbd3* and *Sall4*
585 targeting required one round. For protein depletion, cells were treated with 500μM Auxin or
586 500μM dTAG-13 in standard culture media. All HALOTag-fusion ES cell lines were
587 heterozygous for the HALOTag fusion, i.e. HALO/+, and verified by western blotting.
588

Gene	**gRNA**	**Sequence (5' -- 3')**
Chd4	gRNA1	GGTGGAGGTGGATATCACTC
Mbd3 A3xF	gRNA1	TTCTCACGCGTCACTCGCTC
Mbd3	gRNA2	CAGCCATTCCCTGGAAGTAC
Sall4	gRNA1	AATAAGATTGCTGTCAGCTA
Sall4	gRNA2	AAGATTGCTGTCAGCTAAGG
Nanog	gRNA1	AACTACTCTGTGACTCCACC
Sox2	gRNA1	TGCCCCTGTCGCACATGTGA
Klf4	gRNA2	GTGGGTCACATCCACTACGT

589 **Table 1. gRNA sequences used for gene targeting**
590
591 **Nuclear extract fractionation and western blotting**
592 Nuclear fractionation was carried out as described (Gillotin, 2018). Briefly, cells were
593 collected in ice-cold PBS and pelleted in a refrigerated centrifuge. The cell pellet was lysed by
594 gentle up and down pipetting five times in ice-cold buffer E1 (50 mM HEPES, 140 mM NaCl, 1
595 mM EDTA, 10% glycerol, 0.5% NP40, 0.25% Triton X-100, 1 mM DTT, protease inhibitors). After
596 pelleting and washing in E1 buffer, the pellet was resuspended in ice-cold E2 buffer (10 mM
597 Tris-HCl, 200 mM NaCl, 1 mM EDTA, 0.5 mM EGTA, protease inhibitors) and shaken for 45
598 minutes at 1400rpm at 4°C. The supernatant, representing the nuclear fraction, was collected

599 into a fresh tube. After washing in E2 buffer, the pellet was resuspended in ice-cold E3 buffer
600 (50 mM Tris-HCl, 20 mM NaCl, 1 mM MgCl2, 1% NP-40, protease inhibitors). The resuspended
601 pellet was sonicated at 4°C in a Bioruptor Plus (Diagenode) for 5 minutes, using 30-second
602 ON/30-second OFF cycles at high power. Following sonication, nuclear and chromatin
603 fractions were centrifuged at 16,000 xg at 4°C for 10 minutes. 10µg of extract per lane was
604 used for western blots. Antibodies are listed in Table 2.
605

Antibody target	Raised in	Supplier	Cat #	Dilution (WB)
CHD4	Mouse	Abcam	ab70469	1/5000
CHD4	Rabbit	Abcam	ab72418	1/10000
FLAG	Mouse	Sigma Aldrich	F3165/F1804	1/2000
HA	Mouse	Invitrogen	26183	1/2000
ADNP	Goat	R&D Systems	AF5919	1/2000
Histone H3	Rabbit	Abcam	ab1791	1/5000
MTA2	Mouse	Abcam	ab50209	1/5000
NANOG	Rabbit	Bethyl Labs	A300-387A	1/2000
SOX2	Rat	E-bioscience	14-9811-82	1/2000
Lamin B1	Rabbit	Abcam	ab133741	1/10000
Mouse IgG	Rabbit	Invitrogen	A16162	1/100
Rabbit IgG	Guinea Pig	Antibodies Online	ABIN101961	1/100
Goat IgG	Rabbit	Abcam	ab6697	1/100
Rat IgG	Rabbit	Abcam	ab6703	1/100
Mouse IgG	Sheep	VWR	NA931V	1/2000
Rabbit IgG	Donkey	VWR	NA934V	1/2000

606 **Table 2. Antibodies used in this study with dilutions used for western blot.**
607
608 **Cell cycle analysis**

609 The cell cycle distributions of auxin (500 μM) or dTAG-13 (500 nM) treated ES cell lines were
610 assessed using propidium iodide (PI) staining coupled with flow cytometry. Approximately
611 200,000 single cells were fixed using 70% ethanol for at least 24 hours before staining. Fixed
612 samples were washed twice in PBS and resuspended in 200 μL of PI solution [50 μg/mL
613 propidium iodide (Invitrogen, P3566) and 50 μg/mL DNase and protease-free RNase A
614 (ThermoScientific, EN0531), diluted in sterile PBS] and incubated overnight at 4°C in the dark.
615 The fluorescent intensity of stained samples was determined using the Attune NxT
616 (Thermofisher) equipped with a 561 nm laser line and a minimum of 10,000 single cell events
617 were recorded. The resulting FCS files were analysed using FlowJo (v10.10) and tested for
618 significance using a mixed-effects model with Dunnett's multiple comparisons correction.
619
620 **Single molecule imaging**
621 ES cells were passaged 24 hours before imaging onto either: No 1.0 35 mm glass bottom
622 dishes (MatTek Corporation P35G-1.0-14-C) or No 1.5 35 mm glass bottom dishes (MatTek
623 Corporation P35G-1.5-14-C) with their surfaces pre-coated in poly-L-ornithine(Sigma Aldrich
624 P4957) for ≥30 minutes at 37°C, followed by three PBS rinses at room temperature, followed
625 by 100μg/ml Laminin (Sigma Aldrich L2020) coating in PBS for >4 hours at room temperature.
626 Cells were labelled on the day of imaging with either 250 nM HaloTag®-PA-JF646 (a gift from L.
627 Lavis, Janelia) for 15 minutes, rinsed twice in PBS and incubated for 20 minutes at 37° C in
628 fresh media. PBS rinsing and 20-minute incubation steps were repeated five more times, and
629 the cells were then imaged in fresh media.
630 Single-molecule tracking was carried out using oblique illumination (Tokunaga et al., 2008)
631 on a custom-built double helix point spread function microscope with a Nikon Eclipse Ti-U
632 inverted microscope body and a box incubator set to 37°C (Carr et al., 2017). Beams were
633 expanded and collimated using Galilean beam expanders, then combined using dichroic
634 mirrors. For 2D imaging, a Nikon 1.49 NA 60× oil immersion objective (CFI Apochromat TIRF
635 60XC Oil) was used to focus excitation beams onto the sample, and the microscope was also
636 set to an internal magnification of 1.5x. For 3D DHPSF imaging, a Nikon 1.27 NA 60x water
637 immersion objective lens (CFI SR Plan Apo IR 60XC WI) was used without internal 1.5x
638 magnification. The emission path of the microscope was also modified to include a fixed
639 double helix phase mask (DoubleHelix, Boulder, CO) in the Fourier domain of the emission
640 path of the microscope (Carr et al., 2017; Pavani et al., 2009) . For long-exposure imaging,
641 control samples were fixed in 4% formaldehyde (v/w) in PBS for 10 minutes at room

642 temperature, rinsed twice with PBS and stored in PBS. Samples were imaged in identical pre-
643 warmed culture media and under identical conditions to live-cell samples. Across all
644 experiments, three separate samples per condition were imaged in a day and all experiments
645 were repeated on at least two separate days for biological replications.
646 Background subtraction with a five-pixel rolling ball radius was carried out on image stacks
647 using open-source software Fiji (Schindelin et al., 2012). Single molecules imaged in 2D were
648 localised using the PeakFit tool within the GDSC Single Molecule Light Microscopy (SMLM)
649 plugin (https://github.com/aherbert/gdsc-smlm, (Etheridge et al., 2022)) for Fiji. Localisations
650 were filtered for precision better than 25 nm. For single molecules imaged in 3D, PeakFit was
651 used as above but with an initial precision threshold of 40 nm and an additional analysis step
652 after this. 2D localisations of DHPSF lobes were paired to generate 3D localisations using
653 DHPSFU (https://github.com/TheLaueLab/DHPSFU). Localisations were then tracked across
654 frames to generate trajectories using custom Python code
655 (https://github.com/wb104/trajectory-analysis). Localisations were connected between two
656 successive frames if they were located within 400 nm of each other.
657 Short-exposure trajectories were segmented into confined and unconfined sub-trajectories
658 using the 4P-algorithm from (Basu et al., 2023). Bound fractions were calculated for a sample
659 based on the number of trajectory frames assigned as being confined, divided by the total
660 number of trajectory frames. Tracks with a residence time shorter than 1.5 seconds were
661 filtered out to reduce the impact of noise on further analysis. The decay curve of residence
662 times for each sample was fitted to a single exponential fit using MATLAB (2018) to yield
663 apparent dissociation rates.
664
665 **RNAseq**
666 Cells were harvested in Trizol Reagent and RNA purified using Zymo Direct-zol columns
667 (Zymo Research) according to manufacturer's instructions. 60-100ng of Ribosomal RNA-
668 depleted mRNA was used for library preparation with the the NEXTflex RapidDirectional RNA-
669 seq kit (Illumina). 100bp paired end (2 x 50bp) sequencing was performed on a NovaSeq S1
670 flowcell at the CRUK Cambridge Institute sequencing facility.
671 Raw data were trimmed using TrimGalore v0.6.4. Reads were indexed and aligned to the
672 unmasked GRC38/mm10 reference genome using the Burrows-Wheeler Aligner (BWA) (Li and
673 Durbin, 2009) . Successful removal of adapter and low-quality bases was assessed using

674 FastQC after trimming. File conversion, sorting, removal of duplicates and mitochondrial
675 reads were performed using samtools (Li et al., 2009) .
676 Read counts for genomic features were summarised using featureCounts (Liao et al.,
677 2014) and a list of the GRC38/mm10 genomic features in a GTF format downloaded from
678 https://www.ensembl.org/ and https://genome.ucsc.edu/cgi-bin/hgTables. Differential
679 expression was analysed using DESeq2 (Love et al., 2014) . Raw expression counts were
680 transformed and normalised to FPKM (fragments per kilobase of transcript per million
681 mapped reads). Simple linear models were used for pairwise comparative analyses between
682 the 0-timepoint and depletion timepoints. An adjusted p-value threshold of 0.05 was used to
683 identify significantly differentially expressed genes. For principal component analysis (PCA)
684 and the generation of correlation matrices vst-transformed data were used within DESeq2.
685 Genes were labelled with their Ensembl and their common gene symbols using the
686 Annotation Hub and ensembldb packages (Rainer et al., 2019) . The ComplexHeatmap
687 package was used for the generation of expression heatmaps (Gu et al., 2016) . Volcano plots
688 were generated using the EnhancedVolcano package. To find enriched gene ontology terms
689 among differentially expressed genes, the enrichGO function of the clusterProfiler R package
690 and the genome-wide annotations were retrieved using the biomaRt package (Yu et al., 2012) .
691
692 **ATAC-seq**
693 100,000 nuclei were used for each reaction using the OMNI-ATAC protocol (Corces et al.,
694 2017) with 10,000 rat nuclei added as a spike-in control. Tagmentation was achieved using
695 pA-Tn5 made in-house for 30 minutes at 37°C on a shaking block. Immediately after
696 incubation DNA was purified using a Zymo DNA Clean and Concentrator Kit (Zymo Research).
697 DNA was then eluted in 21 µL of DNAse/RNAse-free H2O. Barcoding for library preparation
698 was performed by PCR amplification using NEBNext® High-Fidelity 2X PCR Master Mix (New
699 England Biolabs) and NEBNext® index primers for Illumina sequencing. Amplified samples
700 were purified using AMPure SPRI beads (VWR International Ltd) and resuspended in 25 µL of
701 10mM Tris-HCl pH 8.0. The Agilent 4200 TapeStation System with D1000 ScreenTape and
702 D1000 Reagents (Agilent) was used for quantification and fragmentation check of the
703 samples. Equimolar ratios of all samples (7 conditions x 2 biological replicates x 2 technical
704 replicates each) were pooled for 300 bp paired end (2 x150 bp) sequencing performed on a
705 NovaSeq S2 flowcell with the CRUK Cancer Institute sequencing facility.

706 Raw data were trimmed to remove adapter contamination using TrimGalore v0.6.4. Reads
707 were aligned to the GRC38/mm10 reference genome and the Rattus norvegicus/Rnor_6.0
708 genome (spike-in) using the BWA aligner. File conversion, sorting, removal of duplicates and
709 mitochondrial reads were performed using SAMtools (Li et al., 2009) . Fragments up to a 120
710 bp length, which represent nucleosome free regions, were used for further analysis. For
711 visualisation purposes bigwig files were generated using bamCoverage from deepTools
712 (Ramírez et al., 2014) . A scale factor was applied calculated as the number of uniquely
713 mapped rat spike-in reads for each sample divided by the number of uniquely mapped reads
714 in the sample with the lowest count. All replicates were pooled together into a single track
715 using bigWigMerge from UCSC Tools (Kent et al., 2002) . Mean profiles of the signal and
716 heatmaps of these regions were plotted using the ComputeMatrix, plotHeatmap and
717 plotProfile functions from deepTools.
718 Peak calling was performed for ≤120bp fragments using macs2 (Zhang et al., 2008) and
719 applying the -f BAMPE -q 0.05 –nolambda –keep-dup auto parameters. Peak annotation and
720 motif analysis was conducted using the annotatePeaks and findMotifsGenome functions
721 from HOMER (Heinz et al., 2010). Integration of these annotated peaks with RNA-seq gene
722 expression data was conducted using custom R scripts. Differential accessibility analysis was
723 carried out using DiffBind (https://bioconductor.org/packages/DiffBind). Differentially
724 accessible regions were identified in pairwise comparisons to timepoint-0 using the rat
725 aligned reads as a spike-in and an adjusted p-value threshold of 0.05. Chromatin state
726 enrichment analysis for both ADNP and CHD4 differentially accessible regions was
727 performed using ChromHMM (Ernst and Kellis, 2017) , using a predefined chromatin state
728 model generated from E14 mouse ESCs ChIP-seq data (Pintacuda et al., 2017) .
729 To analyse the Tn5 integration sites of the ATAC-seq data the plotFootprint() function in
730 VplotR (Serizay and Ahringer, 2021) was used with the addition of a code in a loop to calculate
731 the normalised version of the cuts by manually dividing by the library size of each merged bam
732 file. To analyse the fragment sizes of the ATAC-seq data that correspond to different
733 nucleosome structure sizes, the plotVmat() function in VplotR was used. The merged reads of
734 different time points of CHD4 depletion were normalised using the native libdepth+nloci
735 option, which normalises the reads using the library depth and the number of loci.
736
737 **Cut&Run and Cut&Tag**

Cut&Run and Cut&Tag were carried out as described (Janssens et al., 2022; Meers et al., 2019). For Cut&Run 100,000 live ES cells were used per reaction, with 10,000 rat nuclei added as a spike-in control. Cut&Tag was performed on 100,000 nuclei per reaction. Antibodies (Table 2) were used at 1/100 dilution. pAG-MNAse and pA-Tn5 were made and purified in-house as described (Meers et al., 2019; Picelli et al., 2014). Plasmids 3XFlag-pA-Tn5-Fl and pAG/MNase were a gift from Steven Henikoff (Addgene plasmids #124601 and #123461, respectively). Library preparation for sequencing was carried out in the CSCI Genomics facility. 300 bp paired-end sequencing was performed on a NovaSeqX 25B flowcell at the CRUK Cancer Institute sequencing facility.

Raw data were trimmed to remove adapter contamination using TrimGalore v0.6.4. Reads were aligned to the unmasked GRC38/mm10 reference genome and the Rattus norvegicus/Rnor_6.0 genome (spike-in) using the BWA. File conversion, sorting, removal of duplicates and mitochondrial reads were performed using SAMtools. For visualisation purposes bigwig files were generated using bamCoverage from deepTools. A scale factor was applied calculated as the number of uniquely mapped rat spike-in reads for each sample divided by the number of uniquely mapped reads in the sample with the lowest count. All replicates were pooled together into a single track using bigWigMerge from UCSC Tools. Mean profiles of the signal and heatmaps of these regions were plotted from these tracks using the ComputeMatrix, plotHeatmap and plotProfile functions from deepTools. Peak calling was performed using macs2 and SEACR (Meers et al., 2019) . SEACR was used in non-control mode with the stringent threshold setting (threshold = 0.01). Input BED files consisted of scaled fragment bedgraphs generated from CUT&RUN data. Scaling was performed using a factor based on the number of uniquely mapped rat spike-in reads for each sample, which was then adjusted relative to the sample with the fewest mapped reads. Motif analysis was conducted using HOMER. Differential accessibility analysis was also carried out using the DiffBind package, incorporating DESeq2 functionality. Differentially bound peaks were identified in pairwise comparisons to timepoint-0 using an adjusted p-value threshold of 0.05. Chromatin state enrichment analysis for differentially bound regions was performed using ChromHMM as for ATAC-seq.

MNase-seq

All MNase experiments, sequencing and data processing were carried out exactly as described (Bornelöv et al., 2018) except that nuclei were digested with 500 U/ml micrococcal nuclease (New England Biolabs) at 24°C for 15 minutes with shaking.

Accession numbers

ATAC-seq: E-MTAB-15037

RNAseq: E-MTAB-15102

nascent RNAseq: E-MTAB-15127

Cut&Run: E-MTAB-15606, E-MTAB-15607

Cut&Tag: E-MTAB-15625

Sall4 Depletion ATAC-seq: E-MTAB-15375

Sall4 Cut&Run: GSE203303

MNase: E-MTAB-6807 (Bornelöv et al., 2018),

Acknowledgments

We are grateful to Nick Owens, Vladimir Teif, Joel Mackay and past and present Hendrich and Laue group members for helpful discussions; to Marco Trizzino for support and to the CSCI facilities for expert technical assistance.

Funding

This work was supported by PhD studentships from Wolfson College, Cambridge to A.K., from AstraZeneca to O.O. and from the Medical Research Council to D.S., and by grants from the Medical Research Council to B.D.H. (MR/X018342/1 and MR/Y000595/1) and to E.D.L. (MR/P019471/1 and MR/M010082/1), from the Wellcome Trust to E.D.L. (206291/Z/17/Z), from the Isaac Newton Trust to B.D.H. (17.24(aa)), and core funding from the Wellcome/MRC (203151/Z/16/Z) to the Cambridge Stem Cell Institute.

Author Contributions

AK, OO, IMB, DS and BH created and validated ES cell lines; AK, OO and NR generated sequencing data; AK, OO and RR analysed sequencing data; DS and EDL conducted single molecule imaging experiments and analyses; ML devised methodology; NR, RR, EDL and BH supervised the project and EDL and BH obtained funding. The manuscript was written by BH with input from all other authors.

802

803 **Competing Interests Statement**

804 The authors declare no competing interests.

805

806 **Rererences**

807
808

809 Ahringer J. 2000. NuRD and SIN3 histone deacetylase complexes in development. *Trends Genet*
810 **16**:351–356. doi:10.1016/s0168-9525(00)02066-7

811 Arends T, Dege C, Bortnick A, Danhorn T, Knapp JR, Jia H, Harmacek L, Fleenor CJ, Straign D,
812 Walton K, Leach SM, Feeney AJ, Murre C, O'Connor BP, Hagman JR. 2019. CHD4 is essential
813 for transcriptional repression and lineage progression in B lymphopoiesis. *Proc National Acad*
814 *Sci* **116**:201821301. doi:10.1073/pnas.1821301116

815 Aughey GN, Forsberg E, Grimes K, Zhang S, Southall TD. 2023. NuRD-independent Mi-2 activity
816 represses ectopic gene expression during neuronal maturation. *EMBO Rep* **24**:e55362.
817 doi:10.15252/embr.202255362

818 Basu S, Shukron O, Hall D, Parutto P, Ponjavic A, Shah D, Boucher W, Lando D, Zhang W,
819 Reynolds N, Sober LH, Jartseva A, Ragheb R, Ma X, Cramard J, Floyd R, Balmer J, Drury TA,
820 Carr AR, Needham L-M, Aubert A, Communie G, Gor K, Steindel M, Morey L, Blanco E,
821 Bartke T, Croce LD, Berger I, Schaffitzel C, Lee SF, Stevens TJ, Klenerman D, Hendrich BD,
822 Holcman D, Laue ED. 2023. Live-cell three-dimensional single-molecule tracking reveals
823 modulation of enhancer dynamics by NuRD. *Nat Struct Mol Biol* **30**:1628–1639.
824 doi:10.1038/s41594-023-01095-4

825 Bates LE, Alves MRP, Silva JCR. 2021. Auxin-degron system identifies immediate mechanisms of
826 OCT4. *Stem Cell Rep* **16**:1818–1831. doi:10.1016/j.stemcr.2021.05.016

827 Bornelöv S, Reynolds N, Xenophontos M, Gharbi S, Johnstone E, Floyd R, Ralser M, Signolet J,
828 Loos R, Dietmann S, Bertone P, Hendrich B. 2018. The Nucleosome Remodeling and
829 Deacetylation Complex Modulates Chromatin Structure at Sites of Active Transcription to Fine-
830 Tune Gene Expression. *Mol Cell* **71**:56-72.e4. doi:10.1016/j.molcel.2018.06.003

831 Bracken AP, Brien GL, Verrijzer CP. 2019. Dangerous liaisons: interplay between SWI/SNF,
832 NuRD, and Polycomb in chromatin regulation and cancer. *Gene Dev* **33**:936–959.
833 doi:10.1101/gad.326066.119

834 Burgold T, Barber M, Kloet S, Cramard J, Gharbi S, Floyd R, Kinoshita M, Ralser M, Vermeulen
835 M, Reynolds N, Dietmann S, Hendrich B. 2019. The Nucleosome Remodelling and
836 Deacetylation complex suppresses transcriptional noise during lineage commitment. *EMBO J*
837 **38**:e100788. doi:10.15252/embj.2018100788

838 Carr AR, Ponjavic A, Basu S, McColl J, Santos AM, Davis S, Laue ED, Klenerman D, Lee SF.
839 2017. Three-Dimensional Super-Resolution in Eukaryotic Cells Using the Double-Helix Point
840 Spread Function. *Biophys J* **112**:1444–1454. doi:10.1016/j.bpj.2017.02.023

841 Corces MR, Trevino AE, Hamilton EG, Greenside PG, Sinnott-Armstrong NA, Vesuna S, Satpathy
842 AT, Rubin AJ, Montine KS, Wu B, Kathiria A, Cho SW, Mumbach MR, Carter AC, Kasowski
843 M, Orloff LA, Risca VI, Kundaje A, Khavari PA, Montine TJ, Greenleaf WJ, Chang HY. 2017.
844 An improved ATAC-seq protocol reduces background and enables interrogation of frozen
845 tissues. *Nat Methods* **14**:959–962. doi:10.1038/nmeth.4396

846 Dieuleveult M de, Yen K, Hmitou I, Depaux A, Boussouar F, Dargham DB, Jounier S,
847 Humbertclaude H, Ribierre F, Baulard C, Farrell NP, Park B, Keime C, Carrière L, Berlivet S,
848 Gut M, Gut I, Werner M, Deleuze J-F, Olaso R, Aude J-C, Chantalat S, Pugh BF, Gérard M.
849 2016. Genome-wide nucleosome specificity and function of chromatin remodellers in ES cells.
850 *Nature* **530**:113–116. doi:10.1038/nature16505

851 Dodonova SO, Zhu F, Dienemann C, Taipale J, Cramer P. 2020. Nucleosome-bound SOX2 and
852 SOX11 structures elucidate pioneer factor function. *Nature* **580**:669–672. doi:10.1038/s41586-
853 020-2195-y

854 Ernst J, Kellis M. 2017. Chromatin-state discovery and genome annotation with ChromHMM. *Nat*
855 *Protoc* **12**:2478–2492. doi:10.1038/nprot.2017.124

856 Etheridge TJ, Carr AM, Herbert AD. 2022. GDSC SMLM: Single-molecule localisation
857 microscopy software for ImageJ. *Wellcome Open Res* **7**:241.
858 doi:10.12688/wellcomeopenres.18327.1

859 Feng Q, Zhang Y. 2001. The MeCP1 complex represses transcription through preferential binding,
860 remodeling, and deacetylating methylated nucleosomes. *Gene Dev* **15**:827–832.
861 doi:10.1101/gad.876201

862 Gillotin S. 2018. Isolation of Chromatin-bound Proteins from Subcellular Fractions for Biochemical
863 Analysis. *BIO-Protoc* **8**:e3035. doi:10.21769/bioprotoc.3035

864 Gómez-del Arco P, Perdiguero E, Yunes-Leites PS, Acín-Pérez R, Zeini M, Garcia-Gomez A,
865 Sreenivasan K, Jiménez-Alcázar M, Segalés J, López-Maderuelo D, Ornés B, Jiménez-
866 Borreguero LJ, D'Amato G, Enshell-Seijffers D, Morgan B, Georgopoulos K, Islam ABMMK,
867 Braun T, de la Pompa JL, Kim J, Enriquez JA, Ballestar E, Muñoz-Cánoves P, Redondo JM.
868 2016. The Chromatin Remodeling Complex Chd4/NuRD Controls Striated Muscle Identity and
869 Metabolic Homeostasis. *Cell Metab* **23**:881–892. doi:10.1016/j.cmet.2016.04.008

870 Gourisankar S, Krokhotin A, Wenderski W, Crabtree GR. 2024. Context-specific functions of
871 chromatin remodellers in development and disease. *Nat Rev Genet* **25**:340–361.
872 doi:10.1038/s41576-023-00666-x

873 Grimm JB, English BP, Choi H, Muthusamy AK, Mehl BP, Dong P, Brown TA, Lippincott-
874 Schwartz J, Liu Z, Lionnet T, Lavis LD. 2016. Bright photoactivatable fluorophores for single-
875 molecule imaging. *Nat Methods* **13**:985–988. doi:10.1038/nmeth.4034

876 Gu Z, Eils R, Schlesner M. 2016. Complex heatmaps reveal patterns and correlations in
877 multidimensional genomic data. *Bioinformatics* **32**:2847–2849.
878 doi:10.1093/bioinformatics/btw313

879 Heinz S, Benner C, Spann N, Bertolino E, Lin YC, Laslo P, Cheng JX, Murre C, Singh H, Glass
880 CK. 2010. Simple Combinations of Lineage-Determining Transcription Factors Prime cis-

881 Regulatory Elements Required for Macrophage and B Cell Identities. *Mol Cell* **38**:576–589.
882 doi:10.1016/j.molcel.2010.05.004

883 Hendrich B, Guy J, Ramsahoye B, Wilson VA, Bird A. 2001. Closely related proteins MBD2 and
884 MBD3 play distinctive but interacting roles in mouse development. *Gene Dev* **15**:710–723.
885 doi:10.1101/gad.194101

886 Henikoff JG, Belsky JA, Krassovsky K, MacAlpine DM, Henikoff S. 2011. Epigenome
887 characterization at single base-pair resolution. *Proc National Acad Sci* **108**:18318–18323.
888 doi:10.1073/pnas.1110731108

889 Hota SK, Bruneau BG. 2016. ATP-dependent chromatin remodeling during mammalian
890 development. *Development* **143**:2882–2897. doi:10.1242/dev.128892

891 Janssens DH, Otto DJ, Meers MP, Setty M, Ahmad K, Henikoff S. 2022. CUT&Tag2for1: a
892 modified method for simultaneous profiling of the accessible and silenced regulome in single
893 cells. *Genome Biol* **23**:81. doi:10.1186/s13059-022-02642-w

894 Kent WJ, Sugnet CW, Furey TS, Roskin KM, Pringle TH, Zahler AM, Haussler D. 2002. The
895 Human Genome Browser at UCSC. *Genome Res* **12**:996–1006. doi:10.1101/gr.229102

896 Klein DC, Troy K, Tripplehorn SA, Hainer SJ. 2023. The esBAF and ISWI nucleosome remodeling
897 complexes influence occupancy of overlapping dinucleosomes and fragile nucleosomes in
898 murine embryonic stem cells. *BMC Genom* **24**:201. doi:10.1186/s12864-023-09287-4

899 Kloet SL, Baymaz HI, Makowski M, Groenewold V, Jansen PWTC, Berendsen M, Niazi H, Kops
900 GJ, Vermeulen M. 2015. Towards elucidating the stability, dynamics and architecture of the
901 nucleosome remodeling and deacetylase complex by using quantitative interaction proteomics.
902 *Febs J* **282**:1774–1785. doi:10.1111/febs.12972

903 Kong NR, Bassal MA, Tan HK, Kurland JV, Yong KJ, Young JJ, Yang Y, Li F, Lee JD, Liu Y, Wu
904 C-S, Stein A, Luo HR, Silberstein LE, Bulyk ML, Tenen DG, Chai L. 2021. Zinc Finger Protein
905 SALL4 Functions through an AT-Rich Motif to Regulate Gene Expression. *Cell Reports*
906 **34**:108574. doi:10.1016/j.celrep.2020.108574

907 Kubik S, Bruzzone MJ, Jacquet P, Falcone J-L, Rougemont J, Shore D. 2015. Nucleosome Stability
908 Distinguishes Two Different Promoter Types at All Protein-Coding Genes in Yeast. *Mol Cell*
909 **60**:422–434. doi:10.1016/j.molcel.2015.10.002

910 Kubota T, Nishimura K, Kanemaki MT, Donaldson AD. 2013. The Elg1 Replication Factor C-like
911 Complex Functions in PCNA Unloading during DNA Replication. *Mol Cell* **50**:273–280.
912 doi:10.1016/j.molcel.2013.02.012

913 Lai AY, Wade PA. 2011. Cancer biology and NuRD: a multifaceted chromatin remodelling
914 complex. *Nat Rev Cancer* **11**:588–596. doi:10.1038/nrc3091

915 Lambert SA, Jolma A, Campitelli LF, Das PK, Yin Y, Albu M, Chen X, Taipale J, Hughes TR,
916 Weirauch MT. 2018. The Human Transcription Factors. *Cell* **172**:650–665.
917 doi:10.1016/j.cell.2018.01.029

918 Lando D, Ma X, Cao Y, Jartseva A, Stevens TJ, Boucher W, Reynolds N, Montibus B, Hall D,
919 Lackner A, Ragheb R, Leeb M, Hendrich BD, Laue ED. 2024. Enhancer-promoter interactions

920 are reconfigured through the formation of long-range multiway hubs as mouse ES cells exit
921 pluripotency. *Mol Cell* **84**:1406-1421.e8. doi:10.1016/j.molcel.2024.02.015

922 Lauberth SM, Rauchman M. 2006. A Conserved 12-Amino Acid Motif in Sall1 Recruits the
923 Nucleosome Remodeling and Deacetylase Corepressor Complex. *J Biol Chem* **281**:23922–
924 23931. doi:10.1074/jbc.m513461200

925 Lenz J, Brehm A. 2023. Conserved mechanisms of NuRD function in hematopoetic gene
926 expression. *Enzym* 7–32. doi:10.1016/bs.enz.2023.07.006

927 Li H, Durbin R. 2009. Fast and accurate short read alignment with Burrows–Wheeler transform.
928 *Bioinformatics* **25**:1754–1760. doi:10.1093/bioinformatics/btp324

929 Li H, Handsaker B, Wysoker A, Fennell T, Ruan J, Homer N, Marth G, Abecasis G, Durbin R,
930 Subgroup 1000 Genome Project Data Processing. 2009. The Sequence Alignment/Map format
931 and SAMtools. *Bioinformatics* **25**:2078–2079. doi:10.1093/bioinformatics/btp352

932 Liao Y, Smyth GK, Shi W. 2014. featureCounts: an efficient general purpose program for assigning
933 sequence reads to genomic features. *Bioinformatics* **30**:923–930.
934 doi:10.1093/bioinformatics/btt656

935 Love MI, Huber W, Anders S. 2014. Moderated estimation of fold change and dispersion for RNA-
936 seq data with DESeq2. *Genome Biol* **15**:550. doi:10.1186/s13059-014-0550-8

937 Lu F, Lionnet T. 2021. Transcription Factor Dynamics. *Cold Spring Harb Perspect Biol*
938 **13**:a040949. doi:10.1101/cshperspect.a040949

939 Lu J, Jeong H, Kong N, Yang Y, Carroll J, Luo HR, Silberstein LE, YupoMa, Chai L. 2009. Stem
940 Cell Factor SALL4 Represses the Transcriptions of PTEN and SALL1 through an Epigenetic
941 Repressor Complex. *Plos One* **4**:e5577. doi:10.1371/journal.pone.0005577

942 Martincorena I, Raine KM, Gerstung M, Dawson KJ, Haase K, Loo PV, Davies H, Stratton MR,
943 Campbell PJ. 2017. Universal Patterns of Selection in Cancer and Somatic Tissues. *Cell*
944 **171**:1029-1041.e21. doi:10.1016/j.cell.2017.09.042

945 McDonel P, Costello I, Hendrich B. 2009. Keeping things quiet: Roles of NuRD and Sin3 co-
946 repressor complexes during mammalian development. *Int J Biochem Cell Biology* **41**:108–116.
947 doi:10.1016/j.biocel.2008.07.022

948 Meers MP, Bryson TD, Henikoff JG, Henikoff S. 2019. Improved CUT&RUN chromatin profiling
949 tools. *eLife* **8**:e46314. doi:10.7554/elife.46314

950 Miller A, Ralser M, Kloet SL, Loos R, Nishinakamura R, Bertone P, Vermeulen M, Hendrich B.
951 2016. Sall4 controls differentiation of pluripotent cells independently of the Nucleosome
952 Remodelling and Deacetylation (NuRD) complex. *Development* **143**:3074–3084.
953 doi:10.1242/dev.139113

954 Montibus B, Ragheb R, Diamanti E, Dunn S-J, Reynolds N, Hendrich B. 2023. The Nucleosome
955 Remodelling and Deacetylation complex coordinates the transcriptional response to lineage
956 commitment in pluripotent cells. *Biol Open* **13**:bio060101. doi:10.1242/bio.060101

957 Morris SA, Baek S, Sung M-H, John S, Wiench M, Johnson TA, Schiltz RL, Hager GL. 2014.
958 Overlapping chromatin-remodeling systems collaborate genome wide at dynamic chromatin
959 transitions. *Nat Struct Mol Biol* **21**:73–81. doi:10.1038/nsmb.2718

960 Moshkin YM, Chalkley GE, Kan TW, Reddy BA, Ozgur Z, Ijcken WFJ van, Dekkers DHW,
961 Demmers JA, Travers AA, Verrijzer CP. 2012. Remodelers Organize Cellular Chromatin by
962 Counteracting Intrinsic Histone-DNA Sequence Preferences in a Class-Specific Manner. *Mol*
963 *Cell Biol* **32**:675–688. doi:10.1128/mcb.06365-11

964 Mulas C, Kalkan T, Meyenn F von, Leitch HG, Nichols J, Smith A. 2019. Defined conditions for
965 propagation and manipulation of mouse embryonic stem cells. *Development* **146**:dev173146.
966 doi:10.1242/dev.173146

967 Nabet B, Roberts JM, Buckley DL, Paulk J, Dastjerdi S, Yang A, Leggett AL, Erb MA, Lawlor
968 MA, Souza A, Scott TG, Vittori S, Perry JA, Qi J, Winter GE, Wong K-K, Gray NS, Bradner JE.
969 2018. The dTAG system for immediate and target-specific protein degradation. *Nat Chem Biol*
970 **14**:431–441. doi:10.1038/s41589-018-0021-8

971 Narlikar GJ, Sundaramoorthy R, Owen-Hughes T. 2013. Mechanisms and Functions of ATP-
972 Dependent Chromatin-Remodeling Enzymes. *Cell* **154**:490–503. doi:10.1016/j.cell.2013.07.011

973 Nishimura K, Fukagawa T, Takisawa H, Kakimoto T, Kanemaki M. 2009. An auxin-based degron
974 system for the rapid depletion of proteins in nonplant cells. *Nat Methods* **6**:917–922.
975 doi:10.1038/nmeth.1401

976 Nishinakamura R, Matsumoto Y, Nakao K, Nakamura K, Sato A, Copeland NG, Gilbert DJ,
977 Jenkins NA, Scully S, Lacey DL, Katsuki M, Asashima M, Yokota T. 2001. Murine homolog of
978 SALL1 is essential for ureteric bud invasion in kidney development. *Development* **128**:3105–
979 3115. doi:10.1242/dev.128.16.3105

980 Nocente MC, Karamitsos AM, Drouineau E, Soleil M, Albawardi W, Dulary C, Ribierre F, Picaud
981 H, Alibert O, Acker J, Kervella M, Aude J-C, Gilbert N, Ochsenbein F, Chantalat S, Gérard M.
982 2024. cBAF generates subnucleosomes that expand OCT4 binding and function beyond DNA
983 motifs at enhancers. *Nat Struct Mol Biol* **31**:1756–1768. doi:10.1038/s41594-024-01344-0

984 O'Shaughnessy-Kirwan A, Signolet J, Costello I, Gharbi S, Hendrich B. 2015. Constraint of gene
985 expression by the chromatin remodelling protein CHD4 facilitates lineage specification.
986 *Development* **142**:2586–2597. doi:10.1242/dev.125450

987 Ostapcuk V, Mohn F, Carl SH, Basters A, Hess D, Iesmantavicius V, Lampersberger L, Flemr M,
988 Pandey A, Thomä NH, Betschinger J, Bühler M. 2018. Activity-dependent neuroprotective
989 protein recruits HP1 and CHD4 to control lineage-specifying genes. *Nature* **557**:739–743.
990 doi:10.1038/s41586-018-0153-8

991 Pantier R, Chhatbar K, Quante T, Skourti-Stathaki K, Cholewa-Waclaw J, Alston G, Alexander-
992 Howden B, Lee HY, Cook AG, Spruijt CG, Vermeulen M, Selfridge J, Bird A. 2021. SALL4
993 controls cell fate in response to DNA base composition. *Mol Cell* **81**:845-858.e8.
994 doi:10.1016/j.molcel.2020.11.046

995 Pavani SRP, Greengard A, Piestun R. 2009. Three-dimensional localization with nanometer
996 accuracy using a detector-limited double-helix point spread function system. *Appl Phys Lett*
997 **95**:021103. doi:10.1063/1.3158923

998 Picelli S, Björklund ÅK, Reinius B, Sagasser S, Winberg G, Sandberg R. 2014. Tn5 transposase
999 and tagmentation procedures for massively scaled sequencing projects. *Genome Res* **24**:2033–
1000 2040. doi:10.1101/gr.177881.114

1001 Pierson TM, Otero MG, Grand K, Choi A, Graham JM, Young JI, Mackay JP. 2019. The NuRD
1002 complex and macrocephaly associated neurodevelopmental disorders. *Am J Medical Genetics*
1003 *Part C Seminars Medical Genetics* **181**:548–556. doi:10.1002/ajmg.c.31752

1004 Pintacuda G, Wei G, Roustan C, Kirmizitas BA, Solcan N, Cerase A, Castello A, Mohammed S,
1005 Moindrot B, Nesterova TB, Brockdorff N. 2017. hnRNPK Recruits PCGF3/5-PRC1 to the Xist
1006 RNA B-Repeat to Establish Polycomb-Mediated Chromosomal Silencing. *Mol Cell* **68**:955-
1007 969.e10. doi:10.1016/j.molcel.2017.11.013

1008 Polo SE, Kaidi A, Baskcomb L, Galanty Y, Jackson SP. 2010. Regulation of DNA-damage
1009 responses and cell-cycle progression by the chromatin remodelling factor CHD4. *Embo J*
1010 **29**:3130–3139. doi:10.1038/emboj.2010.188

1011 Pundhir S, Su J, Tapia M, Hansen AM, Haile JS, Hansen K, Porse BT. 2023. The impact of
1012 SWI/SNF and NuRD inactivation on gene expression is tightly coupled with levels of RNA
1013 polymerase II occupancy at promoters. *Genome Res* **33**:332–345. doi:10.1101/gr.277089.122

1014 Ragheb R, Gharbi S, Cramard J, Ogundele O, Kloet S, Burgold T, Vermeulen M, Reynolds N,
1015 Hendrich B. 2020. Differential regulation of lineage commitment in human and mouse primed
1016 pluripotent stem cells by the Nucleosome Remodelling and Deacetylation Complex. *Stem Cell*
1017 *Res* **46**:101867. doi:10.1016/j.scr.2020.101867

1018 Rainer J, Gatto L, Weichenberger CX. 2019. ensembldb: an R package to create and use Ensembl-
1019 based annotation resources. *Bioinformatics* **35**:3151–3153. doi:10.1093/bioinformatics/btz031

1020 Ramírez F, Dündar F, Diehl S, Grüning BA, Manke T. 2014. deepTools: a flexible platform for
1021 exploring deep-sequencing data. *Nucleic Acids Res* **42**:W187–W191. doi:10.1093/nar/gku365

1022 Reid XJ, Low JKK, Mackay JP. 2023. A NuRD for all seasons. *Trends Biochem Sci* **48**:11–25.
1023 doi:10.1016/j.tibs.2022.06.002

1024 Reynolds N, Latos P, Hynes-Allen A, Loos R, Leaford D, O'Shaughnessy A, Mosaku O, Signolet J,
1025 Brennecke P, Kalkan T, Costello I, Humphreys P, Mansfield W, Nakagawa K, Strouboulis J,
1026 Behrens A, Bertone P, Hendrich B. 2012. NuRD Suppresses Pluripotency Gene Expression to
1027 Promote Transcriptional Heterogeneity and Lineage Commitment. *Cell Stem Cell* **10**:583–594.
1028 doi:10.1016/j.stem.2012.02.020

1029 Ru W, Koga T, Wang X, Guo Q, Gearhart MD, Zhao S, Murphy M, Kawakami H, Corcoran D,
1030 Zhang J, Zhu Z, Yao X, Kawakami Y, Xu C. 2022. Structural studies of SALL family protein
1031 zinc finger cluster domains in complex with DNA reveal preferential binding to an AATA
1032 tetranucleotide motif. *J Biol Chem* **298**:102607. doi:10.1016/j.jbc.2022.102607

1033 Saotome M, Poduval DB, Grimm SA, Nagornyuk A, Gunarathna S, Shimbo T, Wade PA, Takaku
1034 M. 2024. Genomic transcription factor binding site selection is edited by the chromatin
1035 remodeling factor CHD4. *Nucleic Acids Res* **52**:3607–3622. doi:10.1093/nar/gkae025

1036 Schep AN, Buenrostro JD, Denny SK, Schwartz K, Sherlock G, Greenleaf WJ. 2015. Structured
1037 nucleosome fingerprints enable high-resolution mapping of chromatin architecture within
1038 regulatory regions. *Genome Res* **25**:1757–1770. doi:10.1101/gr.192294.115

1039 Schindelin J, Arganda-Carreras I, Frise E, Kaynig V, Longair M, Pietzsch T, Preibisch S, Rueden
1040 C, Saalfeld S, Schmid B, Tinevez J-Y, White DJ, Hartenstein V, Eliceiri K, Tomancak P,
1041 Cardona A. 2012. Fiji: an open-source platform for biological-image analysis. *Nat Methods*
1042 **9**:676–682. doi:10.1038/nmeth.2019

1043 Serizay J, Ahringer J. 2021. Generating fragment density plots in R/Bioconductor with VplotR. *J*
1044 *Open Source Softw* **6**:3009. doi:10.21105/joss.03009

1045 Signolet J, Hendrich B. 2015. The function of chromatin modifiers in lineage commitment and cell
1046 fate specification. *Febs J* **282**:1692–1702. doi:10.1111/febs.13132

1047 Smeenk G, Wiegant WW, Vrolijk H, Solari AP, Pastink A, Attikum H van. 2010. The NuRD
1048 chromatin–remodeling complex regulates signaling and repair of DNA damage. *J Cell Biology*
1049 **190**:741–749. doi:10.1083/jcb.201001048

1050 Sreenivasan K, Rodríguez-delaRosa A, Kim J, Mesquita D, Segalés J, Arco PG, Espejo I, Ianni A,
1051 Croce LD, Relaix F, Redondo JM, Braun T, Serrano AL, Perdiguero E, Muñoz-Cánoves P.
1052 2021. CHD4 ensures stem cell lineage fidelity during skeletal muscle regeneration. *Stem Cell*
1053 *Rep* **16**:2089–2098. doi:10.1016/j.stemcr.2021.07.022

1054 Srivastava D, Mahony S. 2020. Sequence and chromatin determinants of transcription factor
1055 binding and the establishment of cell type-specific binding patterns. *Biochim Biophys Acta*
1056 *(BBA) - Gene Regul Mech* **1863**:194443. doi:10.1016/j.bbagrm.2019.194443

1057 Stevens TJ, Lando D, Basu S, Atkinson LP, Cao Y, Lee SF, Leeb M, Wohlfahrt KJ, Boucher W,
1058 O'Shaughnessy-Kirwan A, Cramard J, Faure AJ, Ralser M, Blanco E, Morey L, Sansó M,
1059 Palayret MGS, Lehner B, Croce LD, Wutz A, Hendrich B, Klenerman D, Laue ED. 2017. 3D
1060 structures of individual mammalian genomes studied by single-cell Hi-C. *Nature* **544**:59–64.
1061 doi:10.1038/nature21429

1062 Tokunaga M, Imamoto N, Sakata-Sogawa K. 2008. Highly inclined thin illumination enables clear
1063 single-molecule imaging in cells. *Nat Methods* **5**:159–161. doi:10.1038/nmeth1171

1064 Wade PA, Jones PL, Vermaak D, Wolffe AP. 1998. A multiple subunit Mi-2 histone deacetylase
1065 from Xenopus laevis cofractionates with an associated Snf2 superfamily ATPase. *Curr Biol*
1066 **8**:843–848. doi:10.1016/s0960-9822(98)70328-8

1067 Watson JA, Pantier R, Jayachandran U, Chhatbar K, Alexander-Howden B, Kruusvee V, Prendecki
1068 M, Bird A, Cook AG. 2023. Structure of SALL4 zinc finger domain reveals link between AT-
1069 rich DNA binding and Okihiro syndrome. *Life Sci Alliance* **6**:e202201588.
1070 doi:10.26508/lsa.202201588

1071 Wilczewski CM, Hepperla AJ, Shimbo T, Wasson L, Robbe ZL, Davis IJ, Wade PA, Conlon FL.
1072 2018. CHD4 and the NuRD complex directly control cardiac sarcomere formation. *Proc*
1073 *National Acad Sci* **115**:201722219. doi:10.1073/pnas.1722219115

1074 Williams CJ, Naito T, Arco PG, Seavitt JR, Cashman SM, Souza BD, Qi X, Keables P, Andrian
1075 UHV, Georgopoulos K. 2004. The Chromatin Remodeler Mi-2β Is Required for CD4
1076 Expression and T Cell Development. *Immunity* **20**:719–733. doi:10.1016/j.immuni.2004.05.005

1077 Wilson BG, Roberts CWM. 2011. SWI/SNF nucleosome remodellers and cancer. *Nat Rev Cancer*
1078 **11**:481–492. doi:10.1038/nrc3068

1079 Wit E de, Nora EP. 2023. New insights into genome folding by loop extrusion from inducible
1080 degron technologies. *Nat Rev Genet* **24**:73–85. doi:10.1038/s41576-022-00530-4

1081 Workman JL, Buchman AR. 1993. Multiple functions of nucleosomes and regulatory factors in
1082 transcription. *Trends Biochem Sci* **18**:90–95. doi:10.1016/0968-0004(93)90160-o

1083 Xi Y, Yao J, Chen R, Li W, He X. 2011. Nucleosome fragility reveals novel functional states of
1084 chromatin and poises genes for activation. *Genome Res* **21**:718–724. doi:10.1101/gr.117101.110

1085 Xue Y, Wong J, Moreno GT, Young MK, Côté J, Wang W. 1998. NURD, a Novel Complex with
1086 Both ATP-Dependent Chromatin-Remodeling and Histone Deacetylase Activities. *Mol Cell*
1087 **2**:851–861. doi:10.1016/s1097-2765(00)80299-3

1088 Yoshida T, Hu Y, Zhang Z, Emmanuel AO, Galani K, Muhire B, Snippert HJ, Williams CJ,
1089 Tolstorukov MY, Gounari F, Georgopoulos K. 2019. Chromatin restriction by the nucleosome
1090 remodeler Mi-2β and functional interplay with lineage-specific transcription regulators control
1091 B-cell differentiation. *Genes Dev* **33**:763–781. doi:10.1101/gad.321901.118

1092 Yu G, Wang L-G, Han Y, He Q-Y. 2012. clusterProfiler: an R Package for Comparing Biological
1093 Themes Among Gene Clusters. *OMICS: A J Integr Biol* **16**:284–287.
1094 doi:10.1089/omi.2011.0118

1095 Zhang W, Aubert A, Segura JMG de, Karuppasamy M, Basu S, Murthy AS, Diamante A, Drury
1096 TA, Balmer J, Cramard J, Watson AA, Lando D, Lee SF, Palayret M, Kloet SL, Smits AH,
1097 Deery MJ, Vermeulen M, Hendrich B, Klenerman D, Schaffitzel C, Berger I, Laue ED. 2016.
1098 The Nucleosome Remodeling and Deacetylase Complex NuRD Is Built from Preformed
1099 Catalytically Active Sub-modules. *J Mol Biol* **428**:2931–2942. doi:10.1016/j.jmb.2016.04.025

1100 Zhang Y, LeRoy G, Seelig H-P, Lane WS, Reinberg D. 1998. The Dermatomyositis-Specific
1101 Autoantigen Mi2 Is a Component of a Complex Containing Histone Deacetylase and
1102 Nucleosome Remodeling Activities. *Cell* **95**:279–289. doi:10.1016/s0092-8674(00)81758-4

1103 Zhang Y, Liu T, Meyer CA, Eeckhoute J, Johnson DS, Bernstein BE, Nusbaum C, Myers RM,
1104 Brown M, Li W, Liu XS. 2008. Model-based analysis of ChIP-Seq (MACS). *Genome Biol*
1105 **9**:R137. doi:10.1186/gb-2008-9-9-r137

1106 Zhong Y, Paudel BP, Ryan DP, Low JKK, Franck C, Patel K, Bedward MJ, Torrado M, Payne RJ,
1107 Oijen AM van, Mackay JP. 2020. CHD4 slides nucleosomes by decoupling entry- and exit-side
1108 DNA translocation. *Nat Commun* **11**:1519. doi:10.1038/s41467-020-15183-2

1109 Zhu F, Farnung L, Kaasinen E, Sahu B, Yin Y, Wei B, Dodonova SO, Nitta KR, Morgunova E,
1110 Taipale M, Cramer P, Taipale J. 2018. The interaction landscape between transcription factors
1111 and the nucleosome. *Nature* **562**:76–81. doi:10.1038/s41586-018-0549-5

1112

Supplemental Figure 1

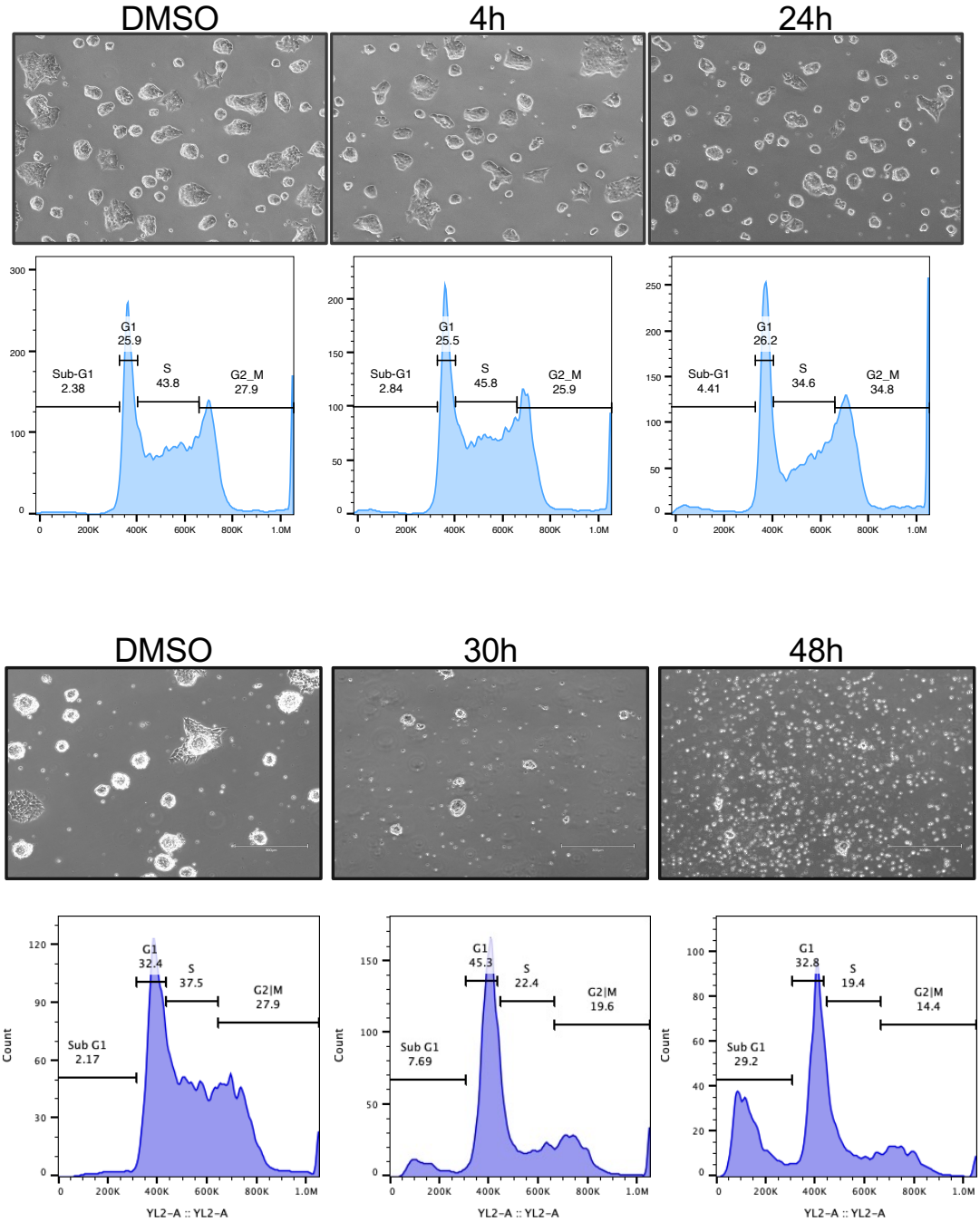

Supplemental Figure 1. Cell cycle arrest and cell death following CHD4 depletion. Phase contrast images and example flow cytometry plots of CHD4-mAID ES cells in 2iL conditions after indicated times of Auxin addition. Cell cycle stage and relative percentage of cells are indicated on the flow cytometry plots.

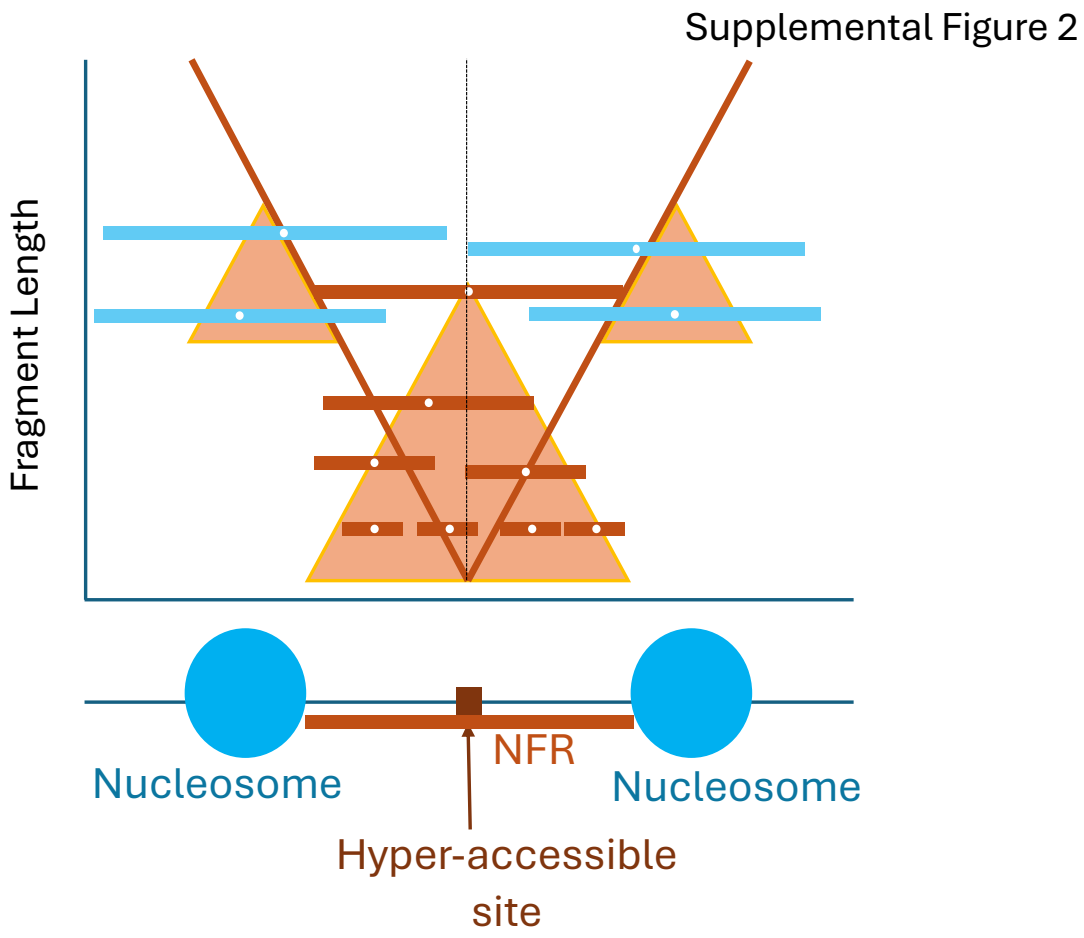

Supplemental Figure 2. Schematic diagram of Vplots. Adapted from (Henikoff et al., 2011) . The Vplot is derived by plotting the midpoint of all recovered fragments (horizontal lines) onto the graph, with midpoint position (white circle) on the x-axis and fragment length on the y-axis. Red lines correspond to reads obtained from fragments with both ends (i.e. Tn5 integration sites) in the NFR, while blue lines represent reads spanning a nucleosome. The vertical dotted line indicates the position of the central hyperaccessible site. The inferred chromatin structure of the locus is shown below.